Geophysical Journal International

Geophys. J. Int. (2020) **222,** 795–814
Advance Access publication 2020 May 01
GJI General Geophysical Methods

doi: 10.1093/gji/ggaa207

AE event rate characteristics of flawed granite: from damage stress to ultimate failure

Jian-Zhi Zhang and Xiao-Ping Zhou

School of Civil Engineering, Chongqing University, Chongqing 400045*, China. E-mail: xiao_ping_zhou@126.com*

Accepted 2020 April 30. Received 2020 March 20; in original form 2019 June 25

SUMMARY

Uniaxial compression tests with combined acousto-optical monitoring techniques are conducted on flawed granite specimens, with the aim of investigating the fracture-related acoustic emission (AE) event rate characteristics at the unstable cracking phase in flawed rocks. The interevent time (IET) function $F(\tau)$ is adopted to interpret the AE time-series from damage stress (σ_{cd}) to ultimate failure, and photographic data are used to evaluate unstable cracking behaviours in flawed granite. The results show that a high AE event rate is always registered but intermittently interrupted by macrofracturing at the unstable cracking phase. The reversed U-shaped curve relation between the AE event rate and the loading time is documented in unstable flawed granite for the first time. The acoustic quiescence has a mechanismic linkage and quantitative correlation with stress drop, and this synchronous acousto-mechanical behaviour is a typical result of the initiation, growth and coalescence of macrocracks initiated from the flaw tips. Moreover, the reactivation and intensification of fracture process zones (FPZs) by increasing loads are the dominant mechanism triggering unstable crack growth in flawed granite.

Key words: Fracture and flow; Geomechanics; Image processing; Instability analysis; Time-series analysis.

1 INTRODUCTION

The fracture-related acoustic emission (AE) activity in natural and engineered materials (such as rocks) is of much concern to seismologists, physicists and engineers. Exploring the temporal rate of the fracture-related AE activity in a stress-induced unstable rock mass enables us to reveal the physical processes of the instability and failure, which has important consequences for natural or induced hazards such as landslides, rockbursts, earthquakes or cliff collapses (Sethna *et al.* 2001; Salje & Dahmen 2014; Colombero *et al.* 2018). A good example elucidating the temporal rate of the AE activity in an unstable rock was recalled from the previous works (Lennartz-Sassinek *et al.* 2014). Based on the experimental observations, subcritical crack growth at the unstable cracking phase of intact Clashach sandstone was described as a characteristic acceleration of the AE event rate and concomitant increased spatial clustering of AE events in the vicinity of an incipient failure plane. This characteristic acceleration of the AE event rate obeys a time-reversed Omori's law [$F(\tau) \sim (t_f - t)^{-p}$ in which $F(\tau)$ characterizes the AE event rate, t_f is the failure time, t is the loading time and p is the power-law exponent] (Main 2000; Kun *et al.* 2013; Goebel *et al.* 2014; Lennartz-Sassinek *et al.* 2014) with the power-law exponent p of approximately 1.0, which underlay the failure forecast. Another excellent example involved the unconfined failure of intact Dionysos marble (Triantis & Kourkoulis 2018). When the failure of intact Dionysos marble was approached, the precursory AE time-series characterizing unstable crack growth was observed to obey the time-reversed Omori's law with the power-law exponent p of 1.20.

The previous experimental studies mainly focused on intact rocks. However, natural rocks usually contain numerous pre-existing flaws, such as joints, faults and fissures (Zhou *et al.* 2018a, 2018b, 2020a; Weng *et al.* 2019). Due to the presence of these natural discontinuities, the failure mechanism of flawed rocks is significantly different from that of intact rocks (Horii & Nemat-Nasser 1985; Bobet & Einstein 1998; Hamiel *et al.* 2006; Zhou *et al.* 2020b). Compared with intact rocks such as Clashach sandstone (Lennartz-Sassinek *et al.* 2014), a multipath failure mode evolving from the pre-existing flaws was commonly observed (Yin *et al.* 2014; Zhou *et al.* 2018a, 2018b, 2020b). This greatly contributes to the rupture progressivity of flawed rocks and the concomitant complexity of the AE characteristics. Previously obtained knowledge of intact rocks cannot be simply applied to interpret the unstable cracking behaviours of flawed rocks. This reason constitutes the necessity to study the AE characteristics in an unstable flawed rock and the associated cracking behaviours. In recent years, a number of experimental studies have been conducted to explore the fracture-related AE characteristics in flawed rocks. For example, Moradian *et al.* (2016) investigated the characteristics of the AE parameters at the different cracking levels in Barre granite containing

two parallel flaws. Huang *et al*. (2017, 2018) adopted the AE monitoring technique to detect the crack propagation behaviours in red sandstone containing a single oval cavity and in granite containing non-coplanar holes, respectively. Wong & Xiong (2018) presented a method for the mesoscale–macroscale interpretations of unconfined fracture processes in Carrara marble containing a single flaw based on the acousto-optical observations. These previous studies mainly focused on the acoustical behaviours in response to the increasing loads and to the momentary strain energy releases occurred in specimens. However, the temporal rate of the AE activity in a stress-induced unstable rock mass was not still comprehensively investigated. As a result, the relation between the AE event rate and the increasing loads (also momentary strain energy releases) at the unstable cracking phase of flawed rocks remains unclear presently.

In this paper, we conduct a set of uniaxial compression tests on flawed granite specimens containing a pair of pre-existing flaws. We monitor the AE activity and the respective load induced in the run-up to ultimate failure. We are mainly concerned with the AE event rate characteristics at the unstable cracking phase. The continuous photographic data captured optically by the VIC-2D digital image correlation (DIC) measurement system are another important experimental output. Correlating the AE event rate characteristics with a growing crack (reflected by photographic data) is considered to be a very good approach to investigate the mechanism triggering unstable crack growth in flawed granite. Uniaxial compression tests performed in this study enable a concomitant and continuous monitoring of acousto-optic-mechanical (AOM) data by the different systems including the AE system, the DIC measurement system, and the material testing system (MTS), and thus the potential correlations among the AOM characteristics in the deforming specimens can be revealed. This paper is organized as follows: Experimental technique and data processing are illustrated in Section 2. Experimental results are analysed in Section 3. The course of the analyses in Section 3 follows the route of solving three important problems: ① How to reliably identify the onset of unstable crack growth? ② What are the AE event rate characteristics at the unstable cracking phase? ③ What are the damage conditions in flawed granite at the unstable cracking phase? To deal with these three problems one by one, Section 3.1 proposes a criterion to identify the time-series from damage stress to ultimate failure in flawed granite, Section 3.2 reveals the AE event rate characteristics in unstable flawed granite and Section 3.3 explores the damage progressions in unstable flawed granite. The quantitative correlations of acoustic quiescence with stress drop in unstable flawed granite are discussed in Section 4. Potential correlations among the AOM characteristics, along with the high-energy AE events generated by the macrofracturing, and the comparison of experimental results between the intact and flawed rocks, are also discussed in Section 4. The implications of the experimental results are described in Section 5, and the main conclusions are finally drawn in Section 6.

2 EXPERIMENTAL TECHNIQUE AND DATA PROCESSING

2.1 Granite specimen and flaw configuration

The samples tested in this study were granite specimens that were cored from the same rock block of a quarry in Zhangzhou city in Fujian Province, China. Laboratory test results indicated that the unit weight, uniaxial compression strength and Young's modulus of the granite are 27.73 kN m^{-3} ± 0.07, 183.56 MPa ± 2.44, and 36.82 GPa ± 0.18, respectively. The prismatic specimen, the size of which was approximately 160 mm × approximately 80 mm × approximately 27 mm (6:3:1), was prepared by saw cutting. Pre-existing flaws, an analogy to natural discontinuities such as joints, faults and fissures in rock masses, were incorporated into the granite specimens, with the aim of guiding mechanically the generation of new cracks. In natural rocks, pre-existing flaws usually appear in sets or groups with similar orientations and characteristics but with a remarkable length discrepancy (Gratchev *et al.* 2016; Zhang *et al.* 2019). Therefore, the flaw configuration in specimens was designed as the two parallel non-isometric pre-existing flaws with a variety of flaw length ratios. The flaw length ratio, R_l, referring to the ratio of the length $2a_2$ of flaw b to the length $2a_1$ of flaw a, as shown in Fig. 1(a), ranges from 1.0 to 3.0 at an interval of 0.5. The centre of flaw a is aligned vertically with the centre of flaw b. The 2-D crack growth is our interpretation. To that end, the flaws run through the specimens (Moradian *et al.* 2016). Fig. 1(a) shows the geometry characteristics for $R_l = 1.0$, where the flaw length $2a_1$ (= $2a_2$) is equal to the ligament length $2b$ (16 mm), and the flaw width is 1.00 mm, the tip radius is about 0.50 mm. The flaw inclination angle α is equal to 45°, enabling this study to account for actual rock mass behaviours in, for example partially benched pillars with angular discontinuities (Esterhuizen *et al.* 2011; Yang *et al.* 2014), on the laboratory scale. Table 1 shows the detailed geometrical parameters for different flaw configurations. Pre-existing flaws were prefabricated using an OMAX water jet. A total of three granite specimens for each flaw length ratio were prepared and tested in the laboratory, aiming at demonstrating the repeatability of the present experiments. In this paper, the artificially created fracture is described as a flaw, while a newly generated macrofracture is designated as a macrocrack (Zhang *et al.* 2019). As such, microcracks refer to cracks that could not be observed unaided with eyes alone.

2.2 Experimental procedure

The specimens were uniaxially loaded in an MTS815 Flex Test GT rock mechanics testing system. A photograph of the test setup is shown in Fig. 1(b). The data were collected with a program called MTS FlexTest 60, which recorded the load, displacement and time electronically. The axial load was imposed on the surface of prismatic specimens at a constant loading rate of 0.05 mm min^{-1} until the specimen failed. The loading rate of 0.05 mm min^{-1} corresponds to the strain rate of about 5.21 × 10^{-6} s^{-1}, which belongs to the quasi-static loading condition (Niu *et al.* 2020).

In addition to the load–displacement measurements, the experimental observations also involved acoustic emissions (Lockner *et al*. 1991; Amitrano *et al.* 2005; Fortin *et al.* 2006; Aggelis *et al.* 2013a; Davidsen *et al.* 2017; Colombero *et al.* 2018; Wang *et al.* 2018), as shown in Fig. 1(c). The AE activities in the deforming specimens were monitored by using the AE system manufactured by PAC (Physical Acoustic Corporation). A total of four AE sensors with a resonance frequency of approximately 150 kHz and a fairly flat response from 0 to 400 kHz were used. The numbers, from 1 to 4, in Fig. 1(a) show the locations of the AE sensors. Among them, Sensors 2 and 3 were attached on the reverse side of the photographed surface. The AEWin software with a hit-based mode was used for acquisition of the AE parameters. For the hit-based mode, the hit is defined from the continuous data file due to the nature

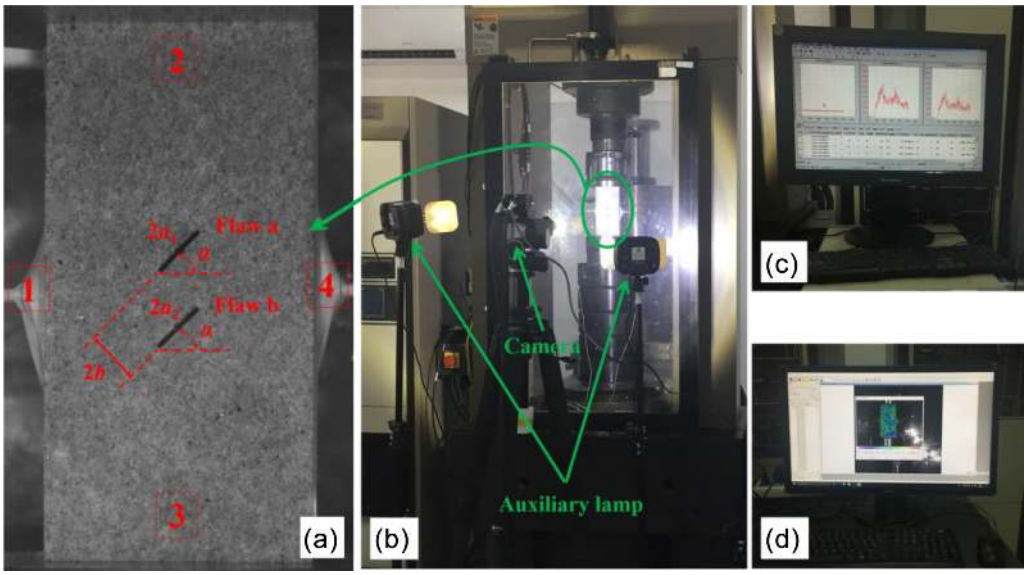

Figure 1. (a) Geometrical parameters of flaw configuration in a double-flawed granite specimen with $R_l = 1.0$ and locations of the attached AE sensors (From 1 to 4), (b) photo of the test setup, (c) AE desktop and (d) digital video desktop. Panel (a), $2a_1$ denotes the length of flaw a, $2a_2$ represents the length of flaw b, α denotes the flaw inclination angle and $2b$ represents the ligament length.

Table 1. Flaw geometry in double-flawed granite specimens.

R_l	$2a_1$ (mm)	$2a_2$ (mm)	$2b$ (mm)	α (°)
1.0	16	16	16	45
1.5	16	24	16	45
2.0	16	32	16	45
2.5	16	40	16	45
3.0	16	48	16	45

of burst signals produced by rock fractures (Moradian *et al.* 2016) and thereby, the data acquisition (DAQ) system saves as much information as is reasonably required. The AE hardware was set up with a pre-amplification of 40 dB, sampling rate of 3 MHz, sample length of 3 k and a bandpass filtration of 20–400 kHz (Moradian *et al.* 2016). To avoid ambient noise (Aggelis *et al.* 2013a), the threshold is set to be 45 dB. Only the AE signal over the threshold of 45 dB can be registered as an AE event. The PDT (peak definition time), HDT (hit definition time) and HLT (hit lockout time) defines the detection of AE events for hit-based mode. Three criteria of PDT = 300 μs, HDT = 800 μs and HLT = 1000 μs were established for the detection of AE events generated from the specimens (Moradian *et al.* 2016). One important factor affecting the detected AE signals is the coupling between the sensors and surfaces of the specimens. To ensure a solid bond, adhesive tape was used to attach the sensors directly to the cleaned specimen surfaces. Vaseline was applied on the surface where the sensors were attached. The efficiency of the coupling and the AE data acquisition parameters was verified by pencil lead break (PLB) and auto sensor testing (AST). In the present experiments, the AE acquisition system was not saturated, and the number of the AE events during the stress drop phase was not undercounted. Every sensor individually detects the AE event as an AE hit. All AE events with at least 1 hit (1 recording sensor) were considered for further processing.

The DIC measurement system in Figs 1(b) and (d) was used to capture the real-time cracking processes of the specimen at a speed of 50 fps (Yin *et al.* 2014; Ji *et al.* 2016; Li & Einstein 2017; Zhang *et al.* 2019; Zhou *et al.* 2020c). The resolution of the camera was 1504 × 1128 pixels, and the length–pixel ratio of the imaging system was calibrated as 0.209 mm pixel^{-1}. To better understand the damage progression characteristics, the area of interest (AOI, the rectangle with black line in Fig. 2a) in the captured image was analysed by DIC software to obtain its strain distributions. The AOI is commonly targeted as the area where significant macrofracturing events such as macrocrack initiation, growth and coalescence, occur, as shown in Fig. 2(b). The basis of the DIC calculation is the matching of speckled patterns at a small square area (called a subset, bounded by the dashed lines in Figs 2a and b) in the AOI between two digital images captured before and after deformation. When the intensity patterns of the two subsets in the two digital images are best matched by DIC, the two subsets are regarded as the same subset, before and after deformation (Lin & Labuz 2013), as shown in Fig. 2. Then, the displacement and the strain between the centre points of the two subsets (namely, the original subset in Fig. 2(a) and the displaced subset in Fig. 2b) are determined. DIC processing continues with a selection of a new subset until the determination of the global strain field in the AOI. One important factor affecting the correlation between the two subsets is the matching of speckle patterns. To ensure good matching, speckles were produced artificially by spraying white and black paint onto the photographed surface before the tests. However, the artificial speckles mask, to some extent, the white patching phenomena (a typical optical effect of fracture process zones, FPZs) that appear on the photographed surface of the specimen. To better detect the white patches, one specimen per flaw length ratio was free of artificial speckles. The calibration of the DIC calculation was completed by Zhang *et al.* (2019).

During the tests, the MTS, the DIC measurement system and the AE system were manually triggered almost simultaneously to obtain the temporal correlation of the AOM data. Despite all this, there still exists the time lapse among different systems. The time lapse between the MTS and the DIC measurement system can be identified through the comparison of the time measurements of the first data points. Moreover, the time lapse between the MTS and the AE system can be defined as the difference of time measurements between the last large stress drop and the last high-energy

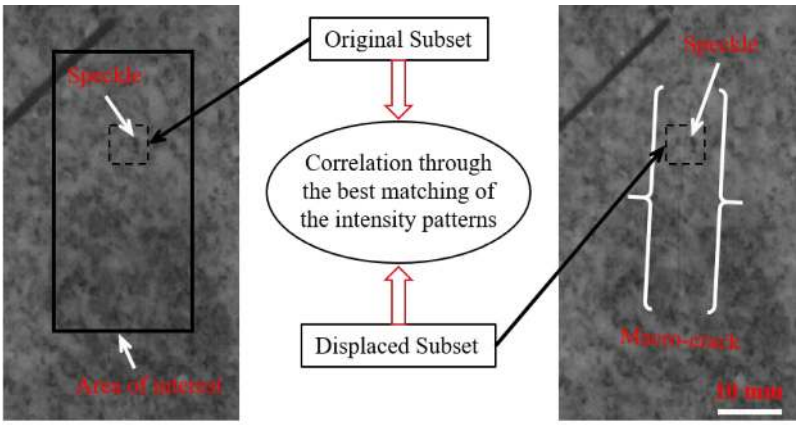

Figure 2. Motion of speckle at the subset in the area of interest (AOI) between (a) the undeformed image and (b) the deformed image with a visible macrocrack, as well as an illustration of the basis of the DIC method.

AE activity. This is because the last large stress drop and the last high-energy AE activity are the two synchronous results of the rock macrofracturing (Huang *et al.* 2017, 2018). The time lapse, albeit small (generally less than 1 s), is incorporated in the data processing to improve the temporal correlation of AOM data. The method used here for improving the temporal correlation of AOM data is not very rigorous, so it should be stated that the correlations among AOM characteristics may be slightly different from what this paper reports.

2.3 Interevent time function $F(\tau)$: an approach to AE data analysis

To study the fracture-related AE event rate characteristics, the approach recently proposed for the representation of AE data (Triantis & Kourkoulis 2018) is used here. This approach introduces the interevent time (IET) function $F(\tau)$, in which τ denotes the mean IET-value for a series of consecutive AE events. To derive the IET function $F(\tau)$, the IET intervals of N consecutive events are used. The IET interval Δt_i is given as follows:

$$\Delta t_i = t_i - t_{i-1},\ i = 2, 3, \ldots \tag{1}$$

where t_i denotes the instant when the ith AE event occurs, and t_{i-1} denotes the instant when the previous AE event occurs.

The mean value, τ_i, of the N interevent time interval Δt_i is determined for each group of N consecutive events as follows:

$$\tau_i = \frac{t_{N+i-1} - t_{i-1}}{N},\ i = 2, 3, \ldots \tag{2}$$

Especially for τ_1, eq. (2) is modified as follows:

$$\tau_1 = \frac{t_N - t_1}{N}. \tag{3}$$

The IET function $F(\tau_i)$ within a given time window between t_{i-1} and t_{N+i-1} is defined as the reciprocal of τ_i, which is given as follows:

$$F(\tau_i) = \tau_i^{-1},\ i = 1, 2, \ldots \tag{4}$$

For the traditional representation of the AE activity in terms of the events per second, the step is, by default, 1 s; thus, there is only one piece of information for each step/second. For the novel representation adopting the IET function $F(\tau)$, the step is in fact the event itself. Taking the function $F(\tau_i)$ and the function $F(\tau_{i+1})$ as characteristic examples, the former reflects the variation in the AE event rate in response to the occurrence of the recent event, and the later characterizes the variation in the AE event rate in response to the appearance of the next event. In this way, the IET function $F(\tau)$ allows for a more informative representation of the AE activity (Triantis & Kourkoulis 2018).

This paper first adopts the IET function $F(\tau)$ to explore the AE activity in a deforming specimen. The analysis is performed on one sensor, rather than the total four sensors. To consider the acoustical information as much fully as possible, the analysed sensor is designated as the one that records the longest AE data set length, regardless of the positions where the sensors are located. In this paper, the longest AE data set lengths among the four sensors for the analysed specimens are 158 301 events ($R_l = 1.0$), 257 244 events ($R_l = 1.5$), 268 317 events ($R_l = 2.0$), 305 955 events ($R_l = 2.5$) and 287 002 events ($R_l = 3.0$), respectively. In the calculation of the IET function $F(\tau)$, the N-value of 100 is used for all tests. The N-value is a relatively small fraction of the total number of AE events recorded (Triantis & Kourkoulis 2018). Moreover, it is noted from eqs (2)–(4) that the last N–1 AE events (i.e. the last 99 AE events in this study) are not defined in terms of the IET function $F(\tau)$, which cause the non-correspondence of acousto-mechanical data during the very last loading steps just before the failure of the specimen. Despite all this, the last acoustic quiescence period for each specimen is still clearly observed, as shown in Fig. 11.

3 EXPERIMENTAL RESULTS

3.1 Acousto-mechanical time-series from damage stress to ultimate failure

The damage stress σ_{cd} commonly represents the onset of unstable crack growth (Ghasemi *et al.* 2019). At σ_{cd}, the critical energy is dissipated by the macrofracturing, and the stress drop is commonly generated. Nonetheless, the stored strain energy in the deforming specimen is still large enough to maintain incrementally intensive or robustly intensive microcracking activities towards failure (Moradian *et al.* 2016; Ghasemi *et al.* 2019). Accordingly, an incrementally high or robustly high AE event rate can always be detected

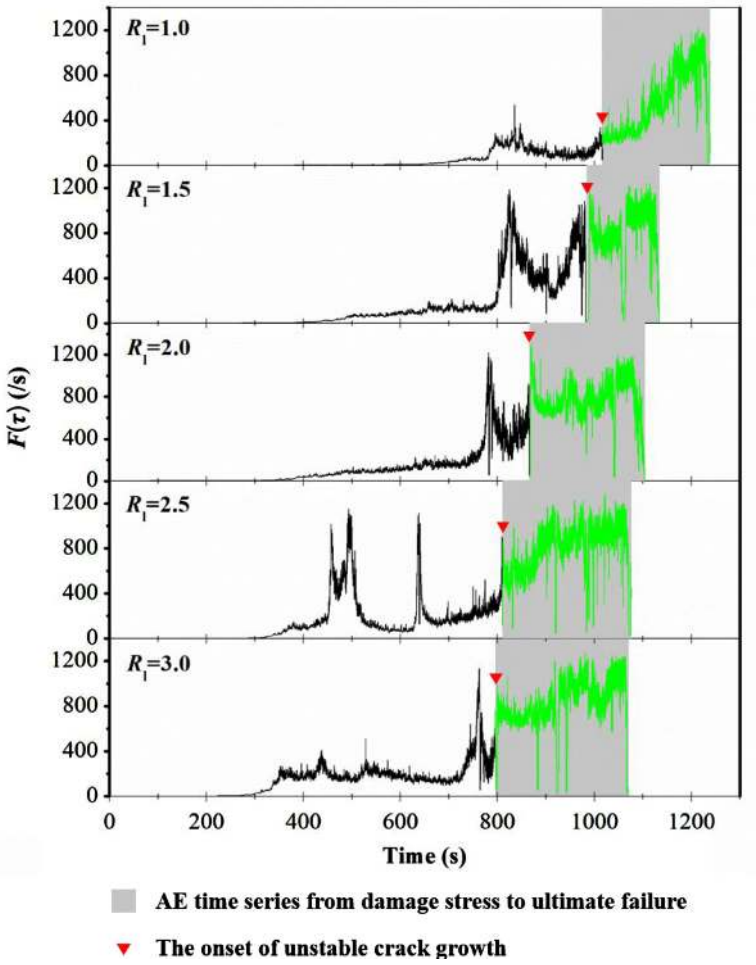

Figure 3. The IET function $F(\tau)$ versus the loading time t for each flaw length ratio in the first experiment. Red 'lower triangles' represent the onset of unstable crack growth, black curves denote the AE time-series before σ_{cd} and green curves in light grey boxes represent the AE time-series from damage stress to ultimate failure.

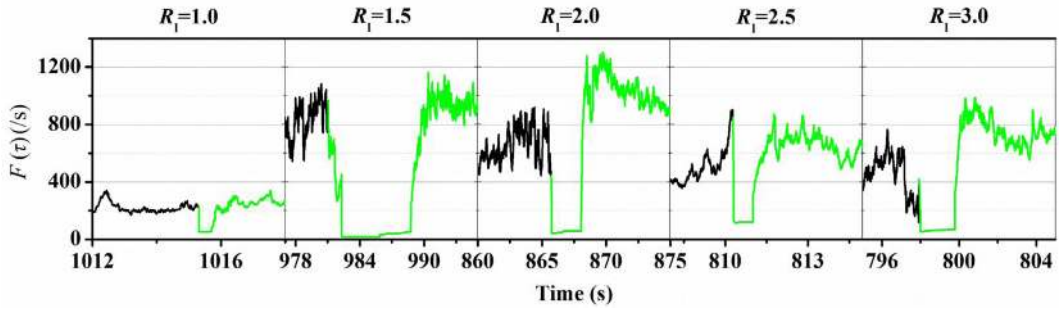

Figure 4. Local amplification of the AE event rate characteristics around the points marked by red 'lower triangles' in Fig. 3. Black curves denote the AE time-series before σ_{cd}, and green curves represent the AE time-series from σ_{cd} onwards.

by the AE sensors after σ_{cd}. This acoustical characteristic serves as a reliable criterion for the identification of AE time-series from damage stress to ultimate failure. The underlying mechanisms can be revealed as the reactivation of FPZs in flawed granite by the increasing loads after σ_{cd}, which are detailed in Section 3.3.

Fig. 3 shows the IET function $F(\tau)$ versus the loading time t for the first experiment of each flaw length ratio. The AE event rate characteristics around the points marked by red 'lower triangles' in Fig. 3 are finely presented in Fig. 4. Initially, for $R_l = 1.0$, an interruption of the AE activity is recorded at 1015.21 s (Fig. 4), displaying that the IET function $F(\tau)$ temporally decreases. The temporal interruption of AE activity is commonly termed acoustic quiescence (Lennartz-Sassinek *et al.* 2014), which is a result of rock macrofracturing occurring at σ_{cd} (Moradian *et al.* 2016). After acoustic quiescence, it is shown that an incrementally high AE event rate can always be detected (Fig. 3) towards failure. For

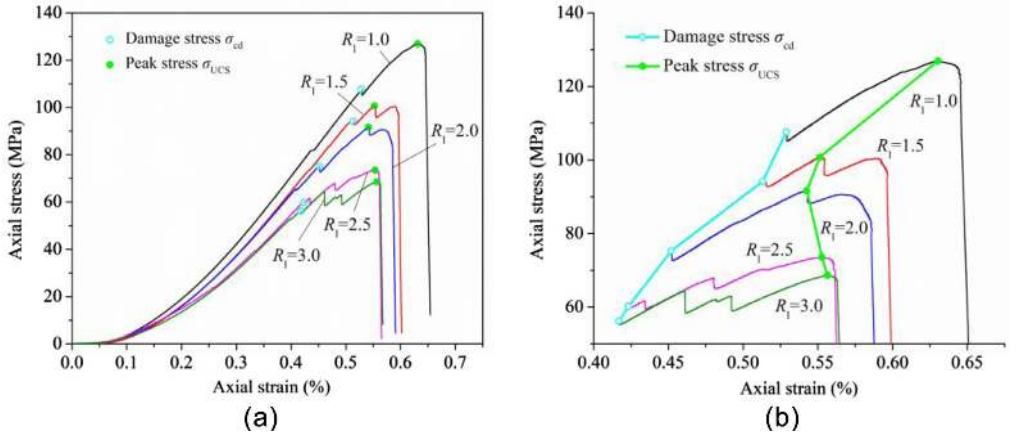

Figure 5. (a) Axial stress–strain curves of the granite specimens with a variety of flaw length ratios in the first experiment, and (b) the axial stress–strain data sets from σ_{cd} onwards and the trends of damage stress σ_{cd} and peak stress σ_{UCS}. The hollow dot denotes damage stress, and the solid dot denotes peak stress.

Table 2. Mechanical and deformation parameters for all of the three parallel experiments of each flaw length ratio.

R_l	σ_{cd} (MPa)	Strain (per cent) at σ_{cd}	σ_{UCS} (MPa)	Peak strain (per cent)	Toughness (J)
1.0	107.61	0.53	126.91	0.63	123.13
	111.72	0.55	127.28	0.62	116.47
	103.90	0.52	128.37	0.63	118.26
1.5	94.17	0.51	100.72	0.55	89.81
	98.89	0.57	103.15	0.64	96.06
	90.46	0.46	117.73	0.57	106.96
2.0	75.29	0.45	91.60	0.54	81.95
	68.97	0.51	80.67	0.65	89.91
	78.12	0.44	95.54	0.54	80.84
2.5	60.16	0.42	73.57	0.55	63.32
	66.59	0.45	81.16	0.52	60.16
	65.46	0.41	90.25	0.54	73.81
3.0	56.20	0.42	68.63	0.56	60.10
	55.04	0.43	66.83	0.55	54.72
	65.00	0.40	67.60	0.48	66.22

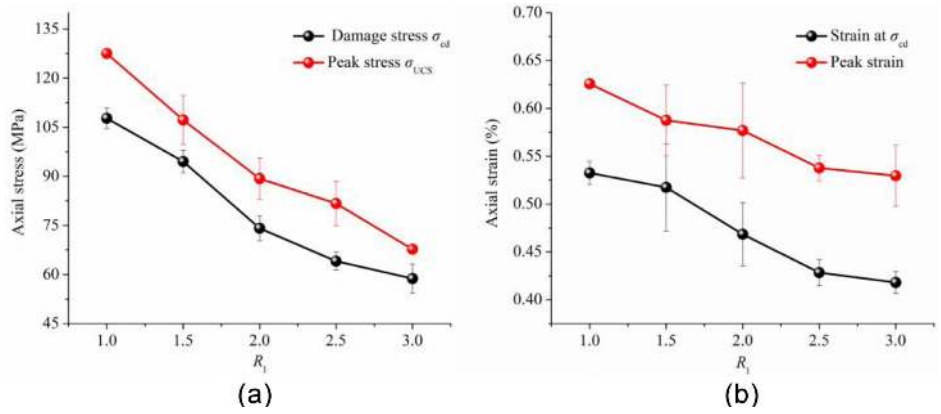

Figure 6. The damage stress σ_{cd} and the peak stress σ_{UCS}, along with the corresponding strains, versus the flaw length ratio R_l.

$R_l = 1.5$, 2.0, 2.5 and 3.0, the acoustic quiescence starts to be registered respectively at 985.87, 865.82, 810.35 and 796.29 s (Fig. 4), and thereafter, a robustly high AE event rate can always be monitored towards failure (Fig. 3). As such, the AE time-series from σ_{cd} onwards can be faithfully identified in the light of the aforementioned criterion. The identified time-series are highlighted by green curves in light-grey boxes in Fig. 3.

Using the correlation of the acousto-mechanical data, the mechanical data set from σ_{cd} onwards can be reliably determined in Fig. 5. Importantly, due to the critical energy release, a remarkable stress drop occurs at σ_{cd} in Fig. 5(a). These characteristic stress drops provide a good validation for the identified time-series. However, the stress drop is just a retrospective validation of the identified time-series, which cannot serve as a criterion for the identification

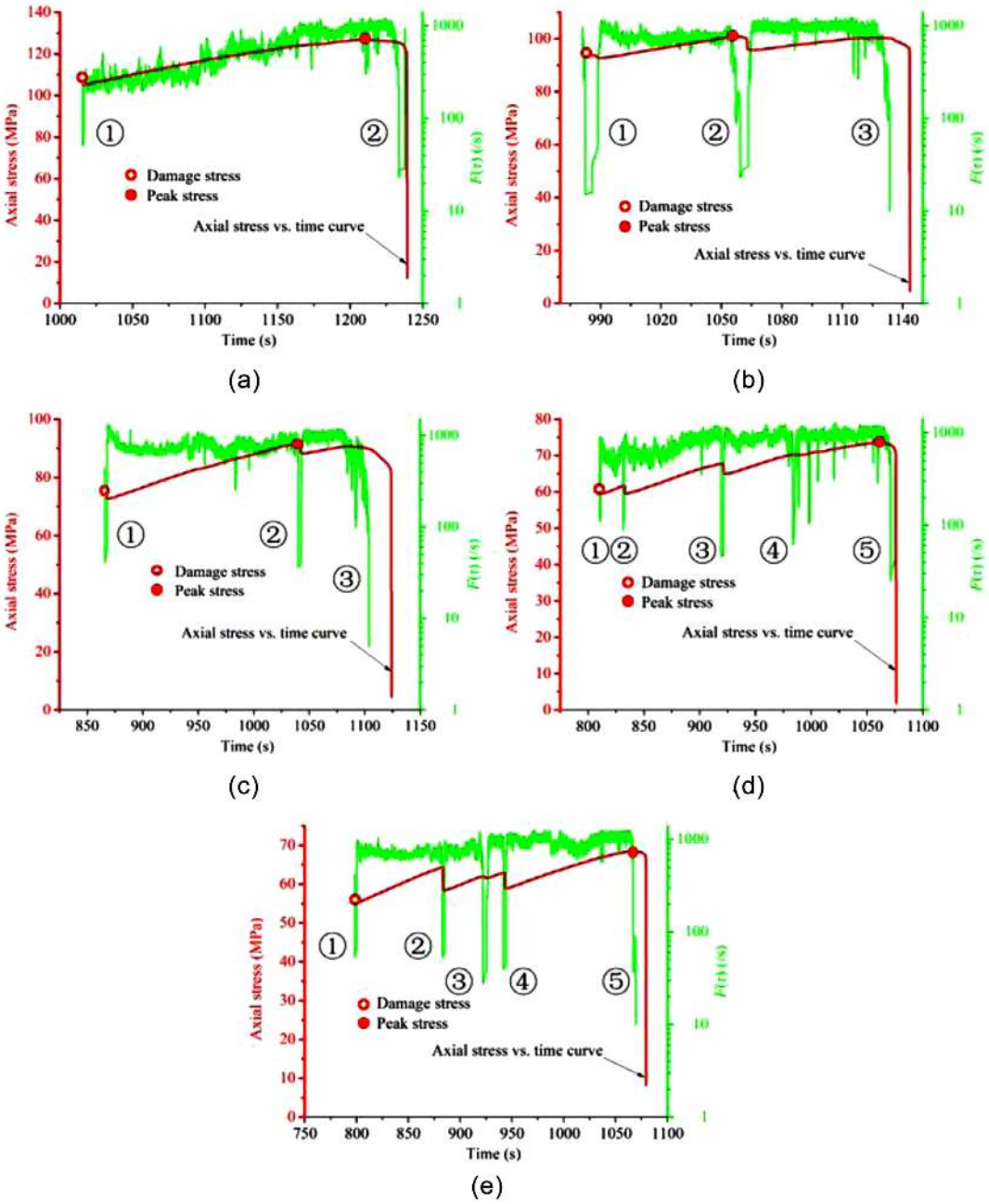

Figure 7. The IET function $F(\tau)$ (green) at the logarithmic scale versus the loading time t in juxtaposition to the respective load (red) induced at the unstable cracking phase for R_l being (a) 1.0, (b) 1.5, (c) 2.0, (d) 2.5 and (e) 3.0. The hollow dot denotes damage stress, and the solid dot denotes peak stress.

of σ_{cd} in flawed granite. This is because the stress drops are initially observed before σ_{cd} (see Fig. 5a), corresponding to the early peaks in the IET function $F(\tau)$ in Fig. 3. The first stress drop is simultaneous with the initiation of the first macrocrack (white line in Figs 8a1–e1). After the first stress drop, a high AE event rate is not detected immediately. This result indicates that after the first stress drop, intensive microcracking activities in flawed granite are not generated and unstable crack growth is not triggered. In fact, this result can be interpreted based on the evolutions of FPZs. After the initiation of the first macrocrack, there are no apparent FPZs that can be reactivated in the deforming specimens. It requires a quite long loading process to form new dominant FPZs. It is therefore suggested that for flawed granite, the identification of σ_{cd} should be based on the indirect monitoring of AE activities but not the direct monitoring of the stress.

Table 2 shows the damage stress σ_{cd} and the peak stress σ_{UCS}, along with the corresponding strains, for all of the three experiments of each flaw length ratio. The above-mentioned criterion is used to identify σ_{cd} in the repeated experiments, and the results are shown in Figs A1(a) and (b) in Appendix A. In this study, σ_{cd} and σ_{UCS}, along with the corresponding strains, are a monotonically decreasing function of the flaw length ratio R_l (Fig. 6). The responses of σ_{cd} and σ_{UCS} to the flaw length ratio R_l may depend on the total length of the two pre-existing flaws. Additionally, the toughness, which is calculated as the area under the load–displacement curve until the displacement is 2 mm (Aggelis *et al.* 2013b),

depends on the stress drop. The specimens with smaller flaw length ratios exhibit notably improved toughness (the last column in Table 2).

3.2 AE event rate characteristics in unstable flawed granite

The rate characteristics of AE time-series from damage stress to ultimate failure are our main concerns. Using the logarithmic scale, the acousto-mechanical time-series from damage stress to ultimate failure are plotted together in Fig. 7. In comparison with the natural scale used in Fig. 3, the logarithmic scale is better suitable for describing the AE event rate characteristics at the unstable cracking phase.

Fig. 7 suggests that the high AE event rate at the unstable cracking phase is intermittently interrupted at specific stress levels. For $R_l = 1.0$, the high AE event rate is interrupted at the very last loading steps, followed by the last large stress drop. This interruption implies the occurrence of the second acoustic quiescence period in $R_l = 1.0$ (the first one has been detected just after σ_{cd} in Fig. 4). It is noted that at the peak stress of 126.91 MPa, only a negligible drop in the AE event rate is captured (Fig. 7a).

Unlike $R_l = 1.0$, an obvious stress drop occurs at the peak stress of 100.72 MPa for $R_l = 1.5$, as shown in Fig. 7b. The robustly high AE event rate is interrupted at this stress point, and as a result, the second acoustic quiescence period for $R_l = 1.5$ appears. This acoustic quiescence is notable, and its quiescent interval reaches 10.21 s. After the second acoustic quiescence, the microcracks evolve violently at a higher speed until the approach to the failure. The last major stress drop is observed to occur concomitantly with the third acoustic quiescence period for $R_l = 1.5$.

For $R_l = 2.0$ (Fig. 7c), the AE event rate characteristics at the unstable cracking phase are rather similar to those for $R_l = 1.5$. The robustly high AE event rate is interrupted by a significant strain energy release at the peak stress of 91.60 MPa, indicating the appearance of the second acoustic quiescence period for $R_l = 2.0$. Shortly thereafter, the microcracks grow violently at a higher speed, which ultimately result in the failure. At the last loading steps, the third apparent acoustic quiescence period is observed.

For $R_l = 2.5$, the interruptions of the AE activity are observed at the stress levels of 61.69 MPa (832.15 s), 67.84 MPa (920.46 s) and 70.30 MPa (984.43 s), instead of at the peak stress of 73.57 MPa (1060.58 s). The acoustic behaviour at the peak stress for $R_l = 2.5$ (Fig. 7d) is similar to that for $R_l = 1.0$, which displays a slight drop in the AE event rate. Since each interruption of the AE activity suggests the occurrence of an acoustic quiescence period, a total of five apparent acoustic quiescence periods are registered for $R_l = 2.5$. When the stress approaches the peak value, some very short acoustic quiescence periods are registered simultaneously with the stress perturbation (the stress perturbation may be related to local grain breakage insides the specimen, Moradian *et al.* 2016; Wong & Xiong 2018; Ghasemi *et al.* 2019).

For $R_l = 3.0$, the AE event rate characteristics at the unstable cracking phase (Fig. 7e) are similar to those for $R_l = 2.5$. A series of apparent interruptions of the AE activity occur, e.g. at the stress levels of 64.32 MPa (882.74 s), 61.99 MPa (922.07 s) and 62.93 MPa (942.09 s). At the peak stress of 68.63 MPa, the AE event rate drops dramatically, indicating that the last acoustic quiescence period occurs. Therefore, for $R_l = 3.0$, a total of five apparent acoustic quiescence periods are found.

The relation between the AE event rate and the loading time at the unstable cracking phase in flawed granite is clearly revealed in Fig. 7. The occurrence of an acoustic quiescence period represents the formation of a reversed U-shaped evolution path of the IET function $F(\tau)$. The reversed U-shaped evolution path of the IET function $F(\tau)$ refers to the observation by which the values of the IET function $F(\tau)$ first increases dramatically and then remains at a high level until a rapid drop occurs. In the present experiments, the time variations in the IET function $F(\tau)$ collapse into one, two, two, four and four reversed U-shaped evolution paths for $R_l = 1.0$, $R_l = 1.5$, $R_l = 2.0$, $R_l = 2.5$ and $R_l = 3.0$, respectively. The reversed U-shaped curve relation between the AE event rate and the loading time at the unstable cracking phase is first documented in this paper, which benefits the understanding of the rupture progressivity. It is concluded that the rupture progressivity of flawed granite is remarkable, and the cracking processes of the specimens with relatively large flaw length ratios exhibit more progressivity than those with small flaw length ratios.

3.3 Unstable crack growth in flawed granite: revealed by optical data

The damage progressions in flawed granite at the unstable cracking phase can be revealed by the white patching phenomena (on the microscopic scale) and the macrofracturing behaviours (on the macroscopic scale). White patches are commonly related to FPZs, namely the clustering of grain-scale microcracks (including grain boundary cracks, intragranular cracks and transgranular cracks) around the flaw tips (Zang *et al.* 2000; Janssen *et al.* 2001; Yin *et al.* 2014). White patches are visible since they occupy a significant contrast in colour patterns in relative to their surrounding area (Becker *et al.* 2010).

Fig. 8 shows the deformed images captured at σ_{cd} and the failure images in the first experiment of each flaw length ratio. For illustration, the macrocracks that immediately propagate at σ_{cd} are labelled by green lines, while the visible initiated cracks are delineated by white lines. White line in Figs 8(a1)–(e1) represents the first macrocrack initiated before σ_{cd}. Sketches illustrating the damage conditions at σ_{cd} and at failure are also presented in Fig. 8. The numbers, from ① to ⑤, mark the sequences of macrofracturing events generating acoustic quiescence (see Fig. 7). The damage conditions corresponding to each of acoustic quiescence periods are detailed in Table 3.

Optical data in Fig. 8 reveal the following four aspects of findings (see the details in Table 3): (1) the tips of the pre-existing flaws (especially the long flaws) become the potential sources of the nucleation of FPZs and the subsequent initiation of macrocracks; (2) prior to the initiation of macrocracks, FPZs always nucleate at the locations where the subsequent macrocracks appear; (3) the flawed granite specimens with relatively large flaw length ratios occupy a remarkable rupture progressivity in relative to those specimens with small flaw length ratios; and (4) the final failure of granite is triggered by the diagonal shear fracture of the long flaw. These optical observations, together with those in the repeated experiments in Figs A1c and d, indicate that the pre-existing flaws are capable of guiding mechanically the formation of macrocracks, which are in good agreements with the previous works (Huang *et al.* 2018; Zhou *et al.* 2018a; Zhang *et al.* 2019; Niu *et al.* 2020).

Especial attention is paid on the damage progressions at σ_{cd}. Apart from the FPZs that have been developed into macrocracks at σ_{cd}, apparent FPZs still survive around the tips of flaws and the tips of formed macrocracks (Fig. 8). These existing FPZs are reactivated

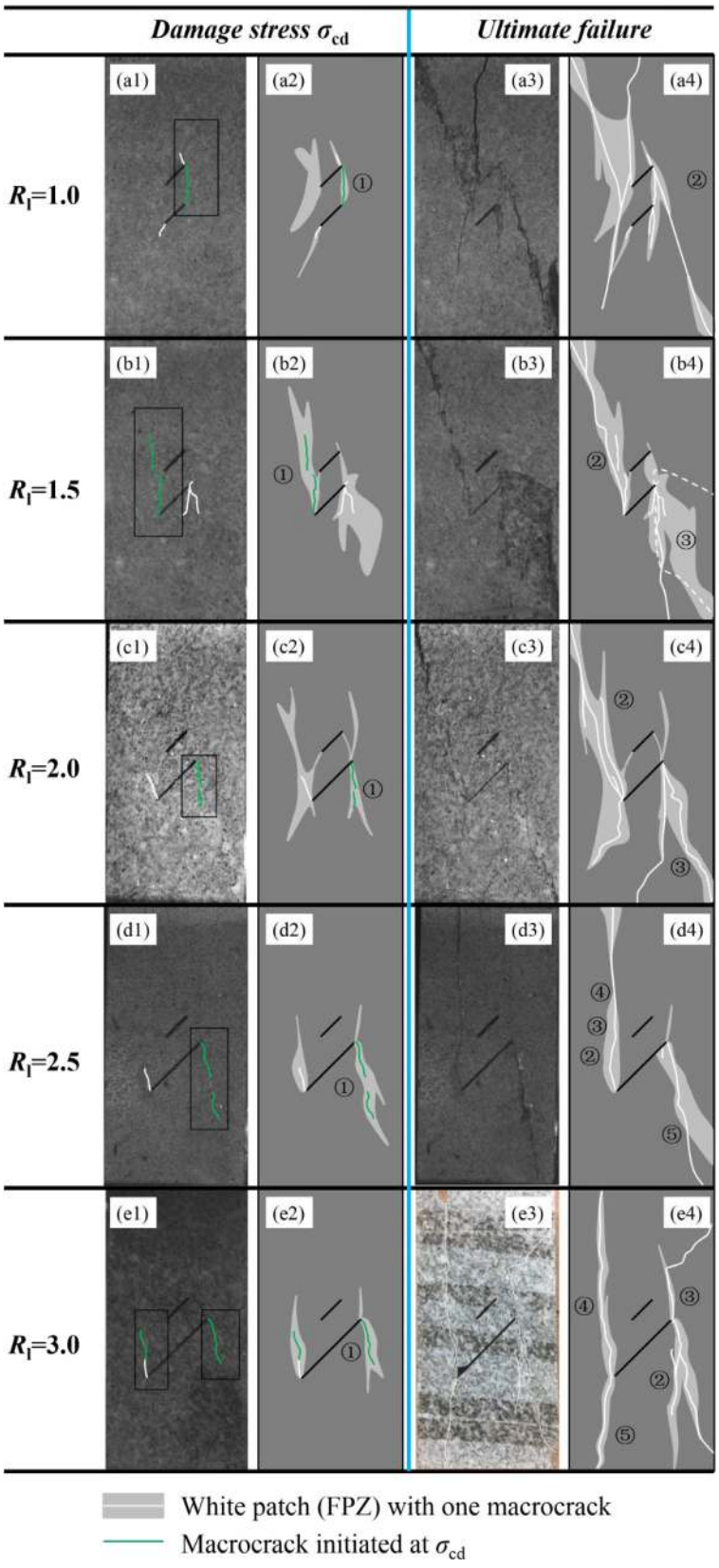

Figure 8. (a1–e1) The deformed images captured at σ_{cd}, (a2–e2) sketches showing the damage conditions (white patching and macrofracturing) at σ_{cd}, (a3–e3) failure images and (a4–e4) sketches showing white patches and macrocracks at the end of tests: (a1–a4) $R_l = 1.0$, (b1–b4) $R_l = 1.5$, (c1–c4) $R_l = 2.0$, (d1–d4) $R_l = 2.5$ and (e1–e4) $R_l = 3.0$. White lines in (a1)–(e1) represent the macrocracks that have been formed before σ_{cd}, and green lines denote the macrocracks that immediately propagate at σ_{cd}. Black boxes in (a1)–(e1) outline the AOIs. The numbers, from ① to ⑤, represent the macrofracturing events generating acoustic quiescence (see Table 3).

Table 3. Damage progressions in flawed granite at specific stress levels.

R_l	No.[a]	Stress (MPa)	Damage conditions
1.0	①	107.61	Tensile antiwing crack occurs at the bridge zone between the upper tip of flaw a and the upper tip of flaw b; Apparent FPZs nucleate around the lower tip of flaw a, and slight FPZs nucleate around the tips of the formed macrocracks
	②	119.75	Nucleated FPZs are expanded and intensified, and dominant macrocracks initiate and propagate to induce ultimate failure
1.5	①	94.17	Tensile antiwing crack initiate from the lower tip of flaw b, extend upwards and coalesces with the far-field crack; Apparent FPZs nucleate around the upper tip of flaw b and the tips of the formed macrocracks
	②	100.72	Nucleated FPZs are expanded and intensified, and tensile antiwing crack initiated from the lower tip of flaw b extend upwards
	③	94.81	Nucleated FPZs are further expanded and intensified; Tensile antiwing crack initiated from the upper tip of flaw b rapidly extends downwards to generate ultimate failure, and meanwhile the surface spalling occurs
2.0	①	75.29	Tensile antiwing crack initiated from the upper tip of flaw b propagates downwards and coalesces with the far-field crack; Apparent FPZs nucleate around the lower tip of flaw b, and slight FPZs nucleate around the upper tip of flaw b
	②	91.60	Tensile antiwing crack initiated from the lower tip of flaw b rapidly grows upwards, and nucleated FPZs are expanded and intensified
	③	78.63	Nucleated FPZs continue to develop; Oblique secondary crack initiates from the upper tip of flaw b and rapidly propagates downwards, which triggers ultimate failure
2.5	①	60.16	Oblique secondary crack initiates from the upper tip of flaw b and coalesces with the downward far-field crack; FPZs nucleate around the tips of long flaw and the tips of formed macrocracks
	②	61.69	Tensile antiwing crack initiated from the lower tip of flaw b grows upwards
	③	67.84	Initiated tensile antiwing crack continues to grows upwards
	④	70.30	Initiated tensile antiwing crack continues to grows upwards
	⑤	69.62	Nucleated FPZs are expanded and intensified; Oblique secondary crack initiated from the upper tip of flaw b rapidly propagates downwards, and ultimate failure is generated
3.0	①	56.20	Tensile antiwing cracks initiated from the lower tip of flaw b propagate upwards, which is simultaneous with the initiation of an oblique secondary crack from the upper tip of flaw b; FPZs nucleate around the tips of long flaw and the tips of formed macrocracks
	②	64.32	Oblique secondary crack initiated from the upper tip of flaw b grows downwards and coalesces with the far-field crack; Nucleated FPZs are expanded and intensified
	③	61.99	Horse tail crack emanates from the upper tip of flaw b
	④	62.93	Tensile antiwing cracks initiated from the lower tip of flaw b continues to propagate upwards; Nucleated FPZs are expanded and intensified
	⑤	68.63	Mixed tensile-shear crack initiates from the lower tip of flaw b, which triggers ultimate failure

[a]The numbering of acoustic quiescence periods.

by the new stress buildup such that the intensive microcracking activities can be generated in flawed granite when the stress increases from σ_{cd}. As a result, a high AE event rate can always be registered after σ_{cd}. The reactivation of FPZs by the stress is the main mechanism for the acoustical criterion used to identify σ_{cd}.

Using DIC, we quantitatively evaluate the strain-induced cracking behaviours at σ_{cd} to reveal the deformation mechanisms in flawed granite. The areas where the macrocracks grow are of interest, so the areas outlined by black boxes in Figs 8(a1)–(e1) are specified as AOIs. Table 4 shows the DIC analysis results of each AOI, including the maximum principal strain ε_1 field and the maximum shear strain ε_{xy} field. The ε_1 field and the ε_{xy} field are, respectively, the dominant mechanisms for the tensile and shear modes cracking. One colour bar applies one analysed specimen.

For $R_l = 1.0$ (Table 4a), FPZs nucleated at the bridge zone between the upper tip of flaw a and the upper tip of flaw b are progressed into macrocracks at σ_{cd} of 107.61 MPa. Geometrically, this macrocrack is a tensile antiwing crack (Zhang *et al.* 2019). At σ_{cd}, ε_1 reaches approximately 0.0157 and ε_{xy} reaches approximately 0.0073. The ratio of $\varepsilon_{xy}/\varepsilon_1$ is equal to approximately 0.46 such that the tensile mode dominates the formation of the coalesced crack (Yin *et al.* 2014).

For $R_l = 1.5$ (Table 4b), tensile antiwing crack, generated within FPZs above the lower tip of flaw b, extends upwards and coalesces with the far-field crack at σ_{cd} of 94.17 MPa. This coalesced crack is dominated by the tensile mode because ε_1 shows significant extensile strain but relatively small ε_{xy} contributes, as shown in Table 4(b). Although ε_{xy} is small, the shear strain localization band is well defined along the path of the coalesced crack.

The deformation mechanisms for $R_l = 2.0$, 2.5 and 3.0 can be revealed in the same way. For $R_l = 2.0$ (Table 4c), tensile antiwing cracks initiated from the upper tip of flaw b propagate downwards and coalesce with the far-field crack at σ_{cd} of 75.29 MPa. The formation of tensile antiwing cracks is a result of the tensile strain release, as shown in Table 4(c). For $R_l = 2.5$ (Table 4d), unstable crack growth is driven by the release of both tensile strain and shear strain. Under such a driving mechanism, an oblique secondary crack initiated from the upper tip of flaw b propagates downwards and coalesces with the far-field crack at σ_{cd} of 60.16 MPa. For $R_l = 3.0$, tensile antiwing cracks initiated from the lower tip of flaw b propagate upwards at σ_{cd} of 56.20 MPa, which is simultaneous with the initiation of an oblique secondary crack from the upper tip of flaw b. At this stress level, a significant tensile strain localizes around the lower tip of flaw b (Table 4e), while tensile strain and shear strain both occur around the upper tip of flaw b (Table 4f).

4 DISCUSSIONS

4.1 Quantitative correlation of acoustic quiescence with stress drop

When the acousto-mechanical data are plotted together against the loading time t, as shown in Fig. 7, there is a near perfect match

Table 4. DIC analysis results including the maximum principal strain ε_1 field and the maximum shear strain ε_{xy} field at σ_{cd} for each flaw length ratio in the first experiment. White lines in the contours represent the macrocracks that have been formed before σ_{cd}, and green lines denote the macrocracks that immediately propagate at σ_{cd}.

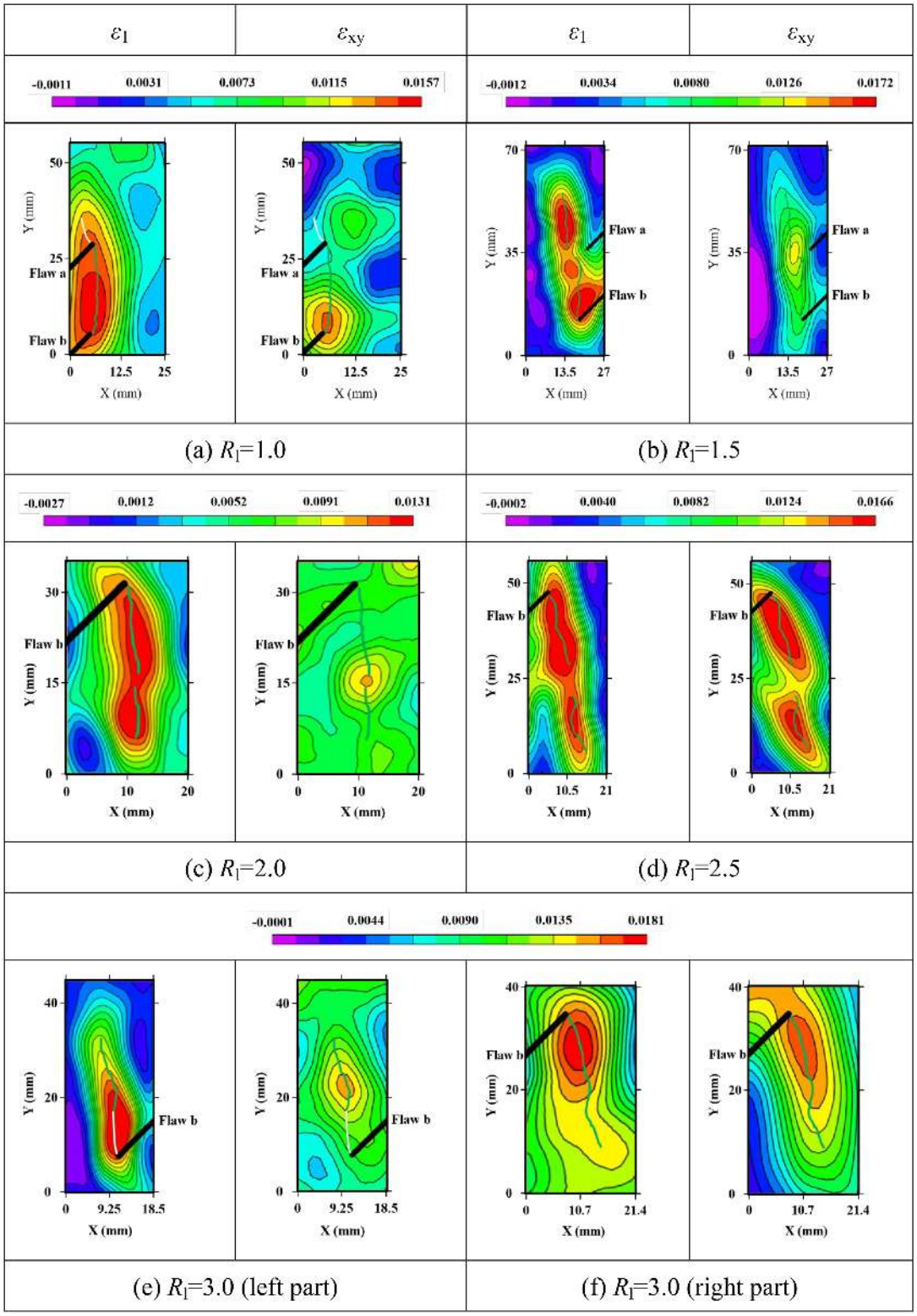

between stress drop and acoustic quiescence. It is reasonably speculated that at the unstable cracking phase, acoustic quiescence connects to stress drop mechanistically. To elucidate the correlation of acoustic quiescence with stress drop, the flawed granite specimen with $R_1 = 1.5$ is analysed in-depth in Figs 9 and 10. Fig. 9 shows the plots of the IET function $F(\tau)$, axial stress, AE counts, AE energy, cumulative AE events, cumulative AE counts and cumulative AE energy versus the loading time t at the unstable cracking

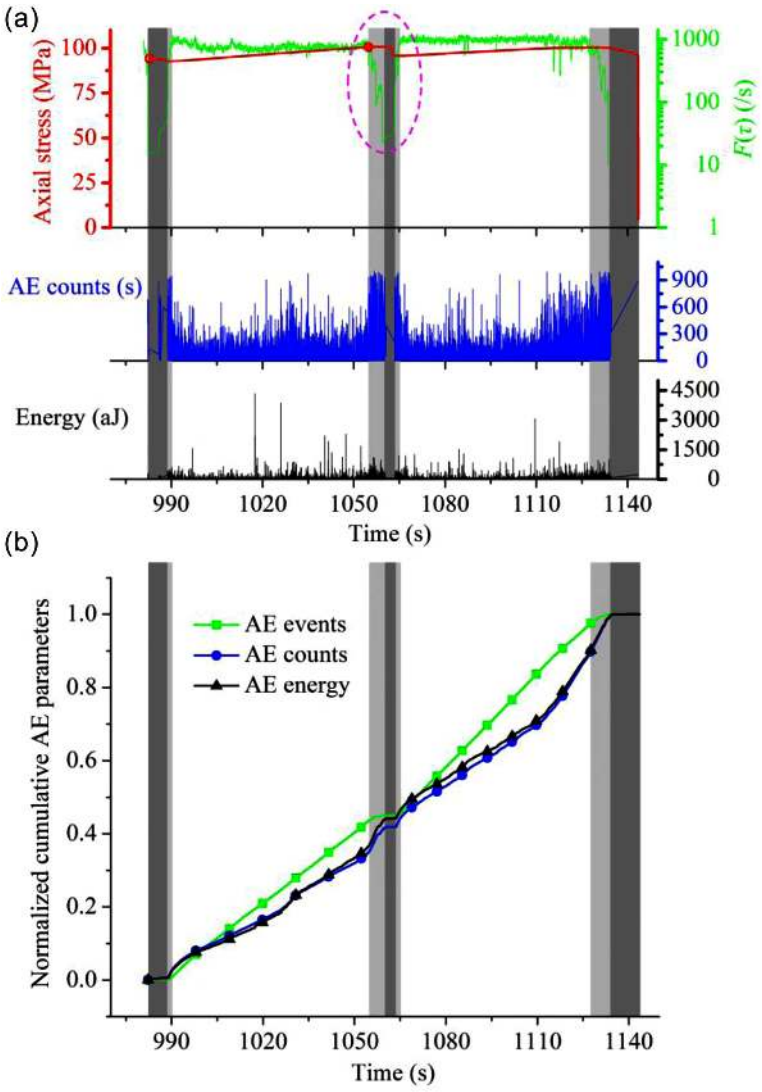

Figure 9. (a) The IET function $F(\tau)$ (green) at the logarithmic scale, AE counts (blue) and energy (black) versus the loading time t, in juxtaposition to the respective load (red) induced at the unstable cracking phase and (b) Normalized cumulative AE parameters, including AE events (green), counts (blue) and energy (black) versus the loading time t for the flawed granite specimen with $R_1 = 1.5$. Cumulative AE parameters are normalized by their maximum records. The light gray region represents the relative acoustic quiescence period (referring to the period during which relatively few AEs are emitted from the specimen), and the dark gray region represents the absolute acoustic quiescence period (referring to the period during which no AEs are recorded by the AE sensors).

phase for $R_1 = 1.5$. The correlation of acoustic quiescence with stress drop over the time window from 1050 to 1070 s (outlined by magenta dashed ellipse in Fig. 9a) is finely analysed in Fig. 10. The axial stress difference, $\Delta\sigma_{1i}$, is defined as the difference between two successive stress measurements. The blue dashed line, located at $\Delta\sigma_{1i} = 0$ in the parametric space of $\Delta\sigma_{1i}$ versus t in Fig. 10, defines the equilibrium state between strain energy dissipation and strain energy absorption in the deforming specimen. When $\Delta\sigma_{1i} > 0$, the stress buildup is dominant such that strain energy absorption prevails over strain energy dissipation. In this state, the associated loading steps are defined as the stress buildup phase, as highlighted by the light blue region in Fig. 10. When $\Delta\sigma_{1i} < 0$, the stress drop is dominant and the corresponding loading steps are defined as the stress drop phase, as highlighted by the grey region. For $\Delta\sigma_{1i} < 0$, strain energy dissipation prevails over strain energy absorption.

Overall, when the stress starts to drop, the AE activity moves into the acoustic quiescence period. However, when the stress is increased again, the AE activity resumes. Taking the second acoustic quiescence period in $R_1 = 1.5$ as an example, the stress initially drops slightly at approximately 1055 s, and relative acoustic quiescence occurs (the left light grey box in Fig. 10). This is followed by an apparent stress drop, along with an absolute acoustic quiescence (dark grey box). After that, the second relative acoustic quiescence is registered simultaneously with the second slight stress drop (the right light grey box). Two types of acoustic quiescence periods, that is the relative acoustic quiescence period and the absolute acoustic quiescence period, are observed in the present experiments. The former refers to the period during which relatively few AEs are emitted from the specimen, while the latter refers to the period during which no AEs are recorded by the AE sensors. A considerable decrease in the slope of the curves of normalized cumulative AE

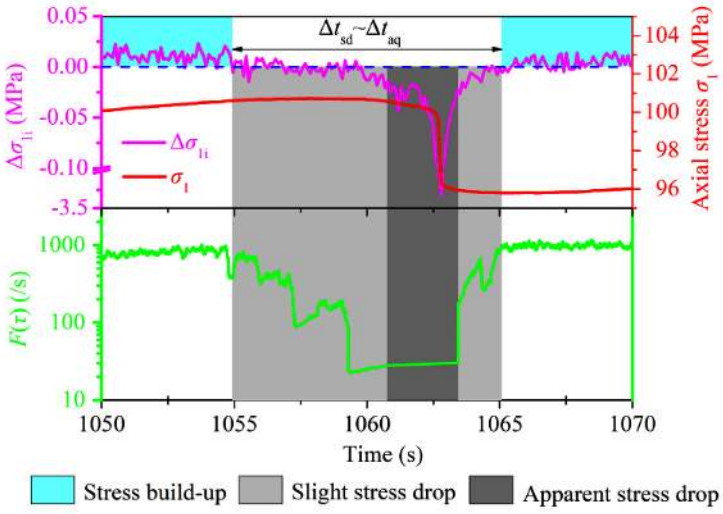

Figure 10. The axial stress difference $\Delta\sigma_{1i}$ (magenta) and the corresponding evolutions of the IET function $F(\tau)$ (green) for the time-series from 1050 to 1070 s (outlined by the magenta dashed ellipse in Fig. 9a) for the flawed granite specimen with $R_l = 1.5$. The blue dashed line located at $\Delta\sigma_{1i} = 0$ represents the equilibrium state between the strain energy dissipation and absorption in the deforming specimen, the light blue region represents the stress buildup, the light grey region represents the slight stress drop and the dark grey region represents the apparent stress drop.

Table 5. The quiescent interval and the corresponding stress drop duration for the first experiment of each flaw length ratio.

R_l	No.[a]	Quiescent interval (s)	Stress drop duration (s)
1.0	①	0.93	0.91
	②	10.46	10.50
1.5	①	8.10	8.13
	②	10.21	10.21
	③	16.17	16.13
2.0	①	2.49	2.42
	②	4.42	4.40
	③	40.13	40.25
2.5	①	1.11	1.17
	②	1.71	1.69
	③	2.66	2.61
	④	2.82	2.79
	⑤	14.38	14.47
3.0	①	2.23	2.31
	②	2.72	2.72
	③	5.26	5.20
	④	3.13	3.12
	⑤	12.98	13.08

[a]The numbering of acoustic quiescence periods.

events versus the loading time t, observed from 1055 to 1065 s in Fig. 9(b), is evident for the acoustic quiescence. Figs 9 and 10 seemingly imply that a slight stress drop corresponds to relative acoustic quiescence, and an apparent stress drop corresponds to absolute acoustic quiescence. For flawed granite, the stress drop commonly occupies a time-consuming process, during which the AE event rate is significantly decreased. That is, the crackling noises in the deforming specimen (Sethna *et al.* 2001; Salje & Dahmen 2014) are less monitored. For $R_l = 1.5$, a total of three acoustic quiescence periods are observed, respectively, at σ_{cd}, at σ_{UCS}, and at the last stress drop. The first quiescent interval (including the relative quiescent interval and the absolute quiescent interval, and the same below) reaches 8.10 s, the second one 10.21 s, and the third one lasts 16.17 s. The corresponding stress drop durations are 8.13, 10.21 and 16.13 s. These experimental observations suggest that the quantitative relation between quiescent interval and stress drop duration can be approximated as:

$$\Delta t_{aq} \sim \Delta t_{sd}, \tag{5}$$

where Δt_{aq} is the quiescent interval, and Δt_{sd} is the stress drop duration. The quantitative relation, that is eq. (5), is firmly supported by more experimental results obtained from the first experiment of each flaw length ratio in Table 5 and Fig. 11.

The acoustic quiescence is attributed to two aspects of mechanisms (Moradian *et al.* 2016): (1) the overlapping of hits, and (2) the blocking of the traversing path of the AE signals by formed macrocracks. Close to the macrofracturing point, the microcracking rate is high, and two microcracks in the rock may occur together so that the second hit from the second crack passes the threshold while the first hit is still being measured. In this state, the number of hits decreases since hits are overlapped instead of being detected individually.

4.2 Correlations among acousto-optic-mechanical (AOM) characteristics

The correlations of AOM characteristics in flawed granite are sketched in Fig. 12, in which the time window from approximately 1055 s to approximately 1065 s for $R_l = 1.5$ is analysed. The red line denotes the time axis, and the thinner red lines and the intervening thicker red line represent the microcracking-dominated damage stage and the macrofracturing-dominated damage stage, respectively. Fig. 12 shows an example of damage progressions from a microcracking-dominated process to a macrofracturing-dominated process, then again to a microcracking-dominated process.

When macrocracks initiate, propagate and coalesce with each other, acoustic quiescence and stress drop are detected immediately and simultaneously. After each macrofracturing, when the stress increases, the microcracking process restarts and the high AE event rate resumes. At this new stress buildup phase, the microcracking

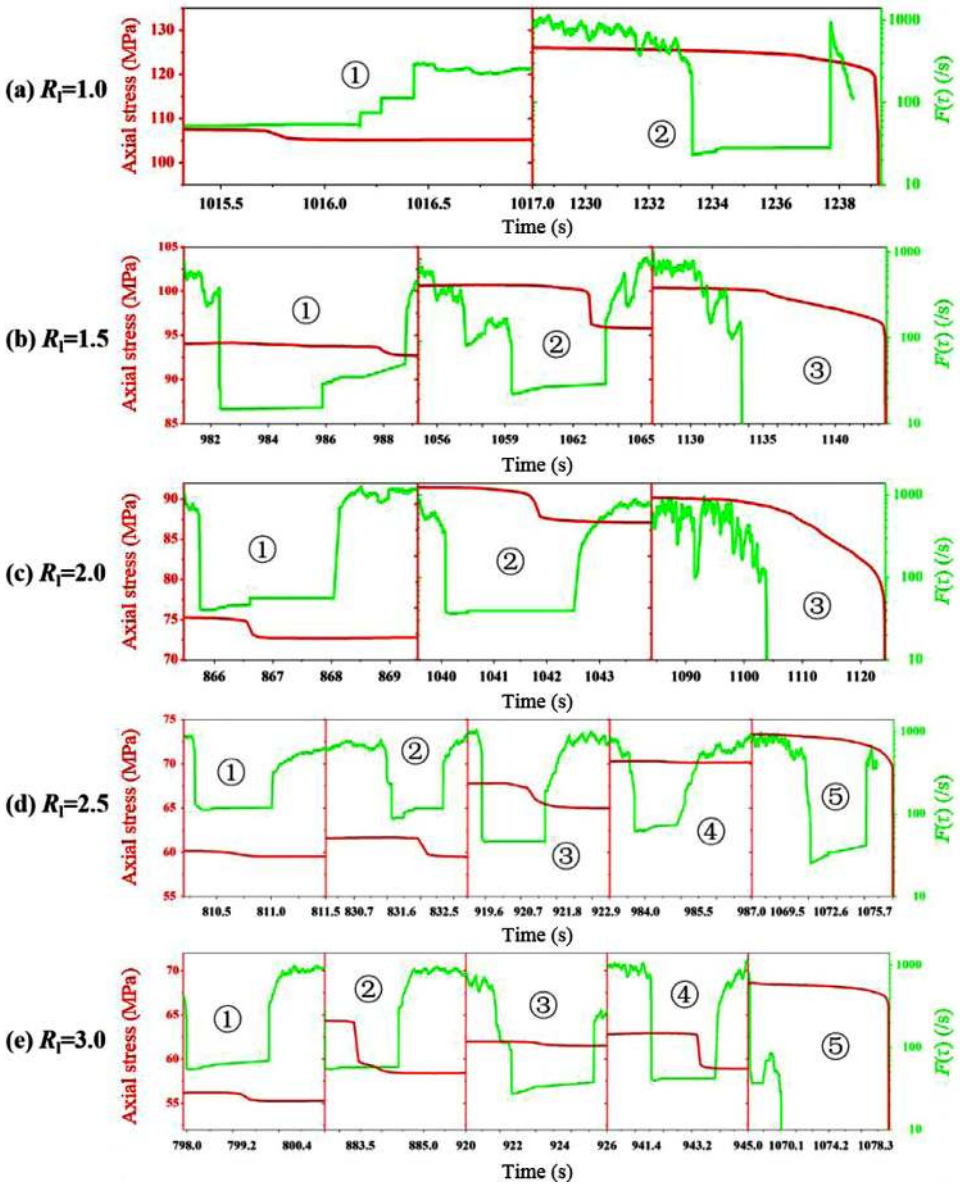

Figure 11. Temporal correlation of acoustic quiescence and stress drop in the first experiment of each flaw length ratio. The numbers, from ① to ⑤, correspond to acoustic quiescence periods in Table 5.

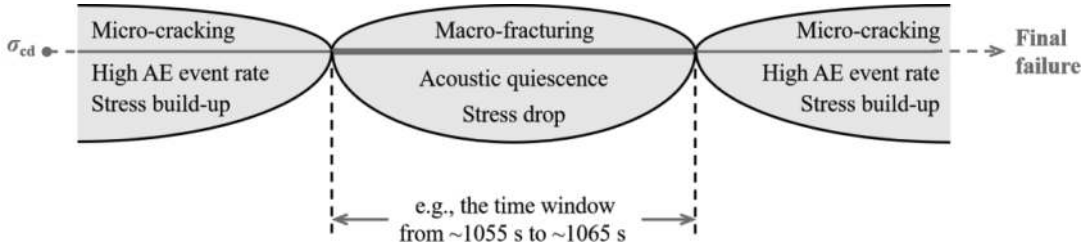

Figure 12. The correlation of AOM characteristics within the time window, for example from ~1055 to ~1065 s, in the flawed granite specimen with $R_l = 1.5$. The red line denotes the time axis, and the thinner red lines and the intervening thicker red line represent the time-series of the microcracking activities and the macrofracturing event, respectively. Ellipses are delineated to distinguish the different time-series from each other.

process restarts, first from the existing FPZs (see Fig. 8), since the FPZs occupy a relatively low bond strength compared with the surrounding 'nearly undamaged' rock matrix. This physical process is directly related to the reactivation of FPZs. As the strain energy increases, the reactivated FPZs are intensified and gradually progressed into new macrocracks. The formation of new macrocracks results in the second trigger of acoustic quiescence and stress drop. Fig. 12 suggests that acoustic quiescence shares the same time window as stress drop, and they are two typical results of rock macrofracturing.

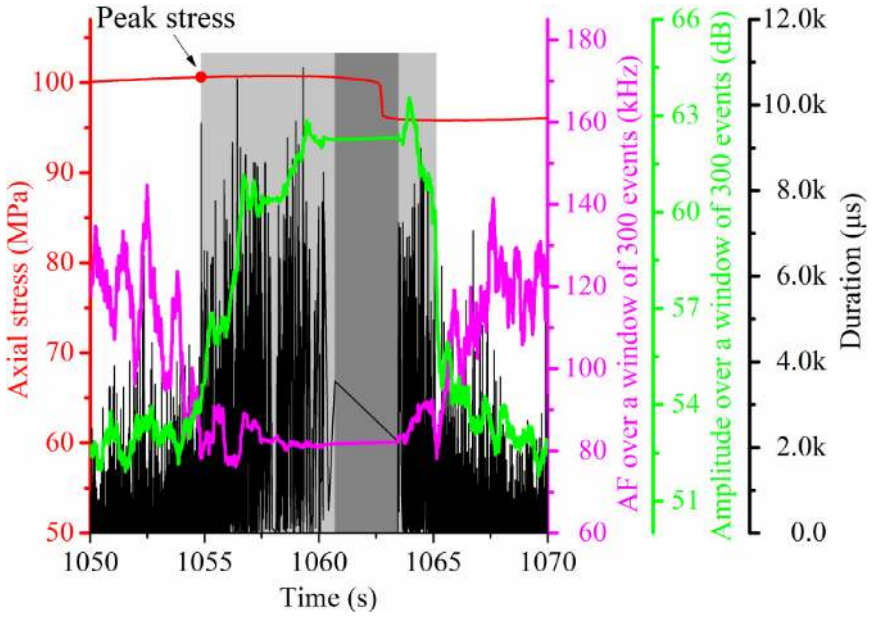

Figure 13. Evolutions of average frequency (AF) (magenta), amplitude (green) and duration (black) in juxtaposition to the respective load (red) induced over a 1050–1070 s time window for a flawed granite specimen with $R_l = 1.5$. The light grey box denotes the relative acoustic quiescence (also slight stress drop), and the dark grey box denotes the absolute acoustic quiescence (also apparent stress drop). The solid dot denotes the peak stress.

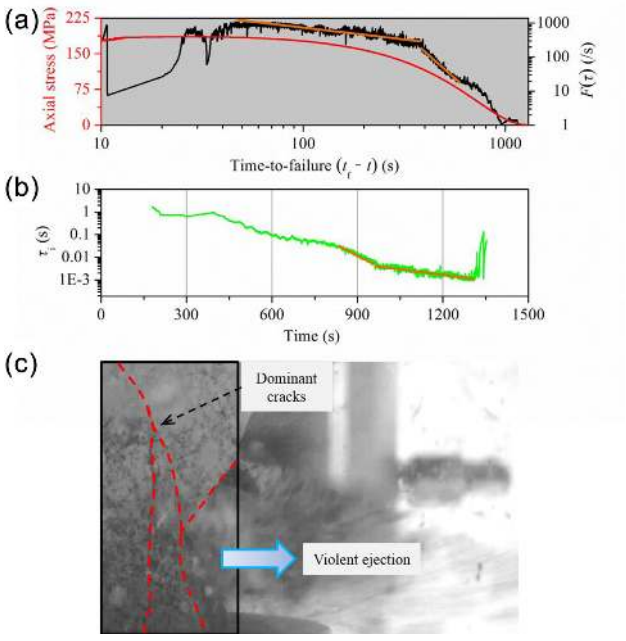

Figure 14. (a) The AE event rate characteristics and the evolutions of axial stress, (b) evolutions of interevent time τ_i and (c) ultimate failure mode of intact granite.

The reactivation and intensification of FPZs in flawed granite are the main mechanisms for the reversed U-shaped curve relation between the AE event rate and the loading time at the unstable cracking phase. The reactivation mechanism of FPZs by the new stress buildup can be related to the strong memory effect (the well-known 'Kaiser effect') of rocks (Main & Meredith 1991; Lennartz-Sassinek *et al.* 2014). The high AE event rate resumed at the new stress buildup phase is attributed to the strong memory of the previously damaged history in FPZs.

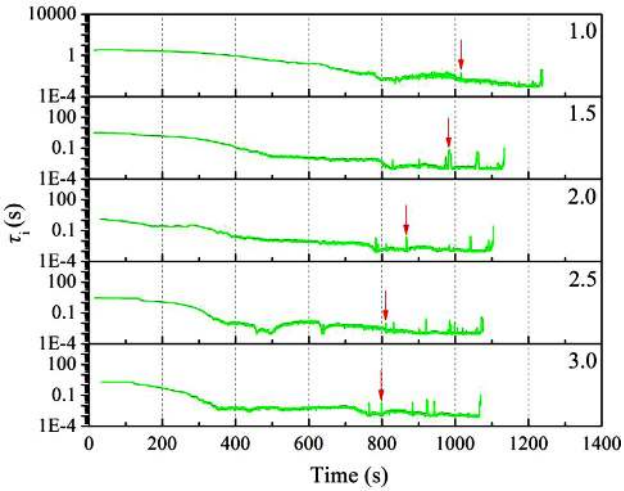

Figure 15. Interevent time τ_i versus time t for each flaw length ratio in the first experiment. Red arrows indicate the onset of unstable crack growth.

4.3 High-energy AE events generated by the macrofracturing

During the relative acoustic quiescence period, the slope of the curves of normalized cumulative AE counts and energy versus the loading time t increases considerably under the conditions that the corresponding AE event rate decreases, as illustrated in Fig. 9(b). This indicates that high-energy AE events, albeit few, are generated during the relative acoustic quiescence period. High-energy AE events are commonly triggered by energetic macrofracturing events such that the detection of high-energy AE events has an important consequence for the forecasting of catastrophe. In fact, more waveform features, such as high amplitude, long duration, and low frequency, are indicative of energetic macrofracturing events. Fig. 13 shows the evolutions of the average frequency (AF), amplitude and duration in juxtaposition to the respective load induced

over the same time window as analysed in Fig. 10. The definition of these AE parameters can be recalled from previous works (Lu *et al.* 2018). In terms of AF and amplitude, we average AF (also amplitude) over a moving window of 300 events; that is AF_i is replaced by the average of all AF_j, $j \in [i-299, i]$ to make the trend more visible. AF generally decreases, while amplitude and duration increase considerably during the relative acoustic quiescence period (light grey box). These waveform features have a robustly temporal correlation with the stress drop so that they are strong indicators of rock macrofracturing. The associated tensile-driven mechanism and the shear-driven mechanism are revealed in Appendix B by the waveform-based analysis approach (Zhang *et al.* 2018).

4.4 Comparison with experimental results obtained from intact rocks

To explore the effects of pre-existing flaws on the rate characteristics of the AE activity, uniaxial compression test was additionally conducted on intact granite specimen. Fig. 14 shows the evolutions of AE event rate, axial stress, IET, along with ultimate failure mode of intact granite. In relative to flawed granite, ultimate failure of intact granite is dictated by sudden propagation of dominant cracks and is commonly violent, as shown in Fig. 14(c). The time-reversed Omori's law (represented by the orange line in Fig. 14a, Amitrano *et al.* 2005; Kun *et al.* 2013; Goebel *et al.* 2014) is tenable for the description of the precursory AE time-series for intact granite. This experimental observation is well consistent with the previous works by Triantis & Kourkoulis (2018). However, a multipath failure mode evolving from the pre-existing flaws (Fig. 8 and Figs A1c and d) is often registered in flawed rocks and as a result, the acceleration of unstable crack growth is frequently interrupted by a series of macrofracturing events. In this state, the acceleration of the AE event rate does not comply with the time-reversed Omori's law. Figs 3 and 7 are evidential for this statement. In addition, the responses of the interevent time τ_i to the increasing loads in intact and flawed granite are different. An approximately exponentially decreasing characteristic of τ_i (represented by the orange line in Fig. 14b) is registered in intact granite but not in flawed granite (Fig. 15). This is attributed to the rupture progressivity of flawed granite. The approximately exponentially decreasing characteristic of τ_i in intact granite is in good agreement with the experimental results obtained from intact Clashach sandstone (Lennartz-Sassinek *et al.* 2014).

The aforementioned distinctions of the AE characteristics between intact and flawed rocks may be related to the differences of rock materials and loading paths. Zhangzhou granite used in this study had a very different modal composition, grain size, porosity and microstructural layering (or inhomogeneity) from Clashach sandstone in Lennartz-Sassinek *et al.* (2014) and Dionysos marble in Triantis & Kourkoulis (2018). These different properties of materials may contribute to the differences of acousto-mechanical behaviours. Moreover, the confining pressure plays an important role in the evolutions of acousto-mechanical behaviours in brittle rocks. The effects of rock materials and loading paths on acousto-mechanical behaviours should be investigated deeply in the future works.

5 IMPLICATIONS OF THE EXPERIMENTAL RESULTS

Based on the systematic analysis of multiple physical field data, the physical processes of the instability in flawed granite have been explored deeply. In specific engineering cases, such as a partially benched pillar (Esterhuizen *et al.* 2011, 2019; Yang *et al.* 2014), the importance of the present experimental results lies in two aspects. First, the damage stress σ_{cd}, also called the long-term strength, for a stressed pillar may be accurately identified based on the real-time rate analysis of AE activities. The damage stress σ_{cd} is an important indicator of the approach to failure because at σ_{cd}, the crack growth in flawed granite has been transited from the stable state to the unstable state. Secondly, the acoustic quiescence may provide a helpful hint to the macrocrack initiation, extension and coalescence and thus, the detection of acoustic quiescence may be conducive to evaluating the working states of a pillar.

6 CONCLUSIONS

In an attempt to elucidate the AE event rate characteristics at the unstable cracking phase of flawed rocks, uniaxial compression tests with combined acousto-optical monitoring techniques are conducted on granite specimens containing a pair of pre-existing flaws. The interevent time (IET) function $F(\tau)$ is adopted to interpret the AE time-series from damage stress to ultimate failure, and the photographic data are used to evaluate unstable cracking behaviours in flawed granite. The main conclusions are drawn as follows:

(1) The damage stress σ_{cd} is reliably identified as the point after which an incrementally high or robustly high AE event rate can always be registered. This result is related to the reactivation and intensification of fracture process zones (FPZs) in flawed granite. After σ_{cd}, the AE event rate characteristics of flawed granite are faithfully described by one single or a series of reversed U-shaped evolution paths, depending on the rupture progressivity. It is the first time that the reversed U-shaped curve relation between the AE event rate and the loading time, observed after σ_{cd}, has been documented.

(2) The interruption of AE activity (termed acoustic quiescence) has a mechanismic linkage and quantitative correlation with stress drop. It is suggested that acoustic quiescence shares the same time window as stress drop, and they are the two typical results of rock macrofracturing. The initiation, growth and coalescence of macrocracks initiated from the flaw tips are the main reasons for acoustic quiescence and concomitant stress drop. Moreover, the reactivation and intensification of FPZs by the increasing loads are the dominant mechanisms triggering unstable crack growth in flawed granite.

Uniaxial tests may result in less realistic results than triaxial tests since the confinements are always present in natural conditions. Nonetheless, the present study can be faithfully applied to account for the actual failure behaviours in important geotechnical structures such as partially benched pillars.

ACKNOWLEDGEMENTS

This work was supported by the National Natural Science Foundation of China (Grant Nos. 51839009 and 51679017).

REFERENCES

Aggelis, D.G., Mpalaskas, A.C. & Matikas, T.E., 2013a. Investigation of different fracture modes in cement-based materials by acoustic emission, *Cem. Concr. Res.*, **48**(2), 1–8.

Aggelis, D.G., Soulioti, D.V., Gatselou, E.A., Barkoula, N.M. & Matikas, T.E., 2013b. Monitoring of the mechanical behavior of concrete with chemically treated steel fibers by acoustic emission, *Constr. Build. Mater.,* **48,** 1255–1260.

Amitrano, D., Grasso, J.R. & Senfaute, G., 2005. Seismic precursory patterns before a cliff collapse and critical point phenomena, *Geophys. Res. Lett.,* **32**(8), L08314.

Becker, D., Cailleau, B., Dahm, T., Shapiro, S. & Kaiser, D., 2010. Stress triggering and stress memory observed from acoustic emission records in a salt mine, *Geophys. J. Int.,* **182**(2), 933–948.

Bobet, A. & Einstein, H.H., 1998. Fracture coalescence in rock-type materials under uniaxial and biaxial compression, *Int. J. Rock Mech. Min. Sci.,* **35**(7), 863–889.

Brooks, Z., Ulm, F.J. & Einstein, H.H., 2013. Environmental scanning electron microscopy (ESEM) and nanoindentation investigation of the crack tip process zone in marble, *Acta Geotech.,* **8**(3), 223–245.

Colombero, C., Comina, C., Vinciguerra, S. & Benson, P., 2018. Microseismicity of an unstable rock mass: from field monitoring to laboratory testing, *J. geophys. Res.,* **123**(2), 1673–1693.

Davidsen, J., Kwiatek, G., Charalampidou, E.M., Goebel, T., Stanchits, S., Rück, M. & Dresen, G., 2017. Triggering processes in rock fracture, *Phys. Rev. Lett.,* **119,** 068501.

Esterhuizen, G.S., Dolinar, D.R. & Ellenberger, J.L., 2011. Pillar strength in underground stone mines in the United States, *Int. J. Rock Mech. Min. Sci.,* **48,** 42–50.

Esterhuizen, G.S., Tyrna, P.L. & Murphy, M.M., 2019. A case study of the collapse of slender pillars affected by through-going discontinuities at a limestone mine in Pennsylvania, *Rock Mech. Rock Eng.,* **52,** 4941–4952.

Fortin, J., Stanchits, S., Dresen, G. & Gueguen, Y., 2006. Acoustic emission and velocities associated with the formation of compaction bands in sandstone, *J. geophys. Res.,* **111,** B10203.

Ghasemi, S., Khamehchiyan, M., Taheri, A., Nikudel, M.R. & Zalooli, A., 2019. Crack evolution in damage stress thresholds in different minerals of granite rock, *Rock Mech. Rock Eng.,* **53,** 1163–1178.

Goebel, T.H.W., Becker, T.W., Sammis, C.G., Dresen, G. & Schorlemmer, D., 2014. Off-fault damage and acoustic emission distributions during the evolution of structurally-complex faults over series of stick-slip events, *Geophys. J. Int.,* **197,** 1705–1718.

Gratchev, I., Dong, H.K. & Chong, K.Y., 2016. Strength of rock-like specimens with preexisting cracks of different length and width, *Rock Mech. Rock Eng.* **49,** 4491–4496.

Hamiel, Y., Katz, O., Lyakhovsky, V., Reches, Z. & Fialko, Y., 2006. Stable and unstable damage evolution in rocks with implications to fracturing of granite, *Geophys. J. Int.,* **167**(2), 1005–1016.

Horii, H. & Nemat-Nasser, S., 1985. Compression-induced microcrack growth in brittle solids: axial splitting and shear failure, *J. geophys. Res.,* **90**(B4), 3105–3125.

Huang, Y.H., Yang, S.Q., Hall, M.R., Tian, W.L. & Yin, P.F., 2018. Experimental study on uniaxial mechanical properties and crack propagation in sandstone containing a single oval cavity, *Arch. Civ. Mech. Eng.,* **18**(4), 1359–1373.

Huang, Y.H., Yang, S.Q., Ranjith, P.G. & Zhao, J., 2017. Strength failure behavior and crack evolution mechanism of granite containing pre-existing non-coplanar holes: experimental study and particle flow modeling, *Comput. Geotech.,* **88,** 182–198.

Janssen, C., Wagner, F., Zang, A. & Dresen, G., 2001. Fracture process zone in granite: a microstructural analysis, *Int. J. Earth Sci.,* **90**(1), 46–59.

Ji, W.W., Pan, P.Z., Lin, Q., Feng, X.T. & Du, M.P., 2016. Do disk-type specimens generate a mode II fracture without confinement?, *Int. J. Rock Mech. Min. Sci.,* **87,** 48–54.

Kun, F., Varga, I., Lennartz-Sassinek, S. & Main, I.G., 2013. Approach to failure in porous granular materials under compression, *Phys. Rev. E,* **88**(6), 062207.

Lennartz-Sassinek, S., Main, I.G., Zaiser, M. & Graham, C.C., 2014. Acceleration and localization of subcritical crack growth in a natural composite material, *Phys. Rev. E,* **90**(5–1), 052401.

Li, B.Q. & Einstein, H.H., 2017. Comparison of visual and acoustic emission observations in a four point bending experiment on Barre Granite, *Rock Mech. Rock Eng.,* **50**(9), 2277–2296.

Li, L.R., Deng, J.H., Zheng, L. & Liu, J.F., 2017. Dominant frequency characteristics of acoustic emissions in white marble during direct tensile tests, *Rock Mech. Rock Eng.,* **50**(5), 1337–1346.

Lin, Q. & Labuz, J.F., 2013. Fracture of sandstone characterized by digital image correlation, *Int. J. Rock Mech. Min. Sci.,* **60,** 235–245.

Lockner, D.A., Byerlee, J.D., Kuksenko, V., Ponomarev, A. & Sidorin, A., 1991. Quasi-static fault growth and shear fracture energy in granite, *Nature,* **350,** 39–42.

Lu, C.P., Liu, Y., Zhang, N., Zhao, T.B. & Wang, H.Y., 2018. In-situ and experimental investigations of rockburst precursor and prevention induced by fault slip, *Int. J. Rock Mech. Min. Sci.,* **108,** 86–95.

Main, I.G., 2000. A damage mechanics model for power-law creep and earthquake aftershock and foreshock sequences, *Geophys. J. Int.,* **142**(1), 151–161.

Main, I.G. & Meredith, P.G., 1991. Stress corrosion constitutive laws as a possible mechanism of intermediate-term and short-term seismic quiescence, *Geophys. J. Int.,* **107**(2), 363–372.

Moradian, Z., Einstein, H.H. & Ballivy, G., 2016. Detection of cracking levels in brittle rocks by parametric analysis of the acoustic emission signals, *Rock Mech. Rock Eng.,* **49**(3), 785–800.

Morgan, S.P., Johnson, C.A. & Einstein, H.H., 2013. Cracking processes in Barre granite: fracture process zones and crack coalescence, *Int. J. Fract.,* **180**(2), 177–204.

Niu, Y., Zhou, X.P. & Berto, F., 2020. Evaluation of fracture mode classification in flawed red sandstone under uniaxial compression, *Theor. Appl. Fract. Mec.,* **107,** 102528.

Salje, E.K.H. & Dahmen, K.A., 2014. Crackling noise in disordered materials, *Annu. Rev. Conden. Ma. P,* **5,** 233–254.

Sethna, J.P., Dahmen, K.A. & Myers, C.R., 2001. Crackling noise, *Nature,* **410,** 242–250.

Triantis, D. & Kourkoulis, S.K., 2018. An alternative approach for representing the data provided by the acoustic emission technique, *Rock Mech. Rock Eng.,* **51**(8), 2433–2438.

Wang, Y., Li, C.H. & Hu, Y.Z., 2018. Experimental investigation on the fracture behavior of black shale by acoustic emission monitoring and CT image analysis during uniaxial compression, *Geophys. J. Int.,* **213**(1), 660–675.

Weng, L., Wu, Z.J. & Liu, Q.S., 2019. Evaluating damage and microcracking behavior of granite using NMR testing under different levels of unconfined compression, *Int. J. Geomech.,* **19**(1), 04018186.

Wong, L.N.Y. & Xiong, Q., 2018. A method for multiscale interpretation of fracture processes in Carrara marble specimen containing a single flaw under uniaxial compression, *J. geophys. Res.,* **123,** 6459–6490.

Yang, S.Q., Jing, H.W., Huang, Y.H., Ranjith, P.G. & Jiao, Y.Y., 2014. Fracture mechanical behavior of red sandstone containing a single fissure and two parallel fissures after exposure to different high temperature treatments, *J. Struct. Geol.,* **69,** 245–264.

Yin, P., Wong, R.H.C. & Chau, K.T., 2014. Coalescence of two parallel pre-existing surface cracks in granite, *Int. J. Rock Mech. Min. Sci.,* **68**(6), 66–84.

Zang, A., Wagner, F.C., Stanchits, S., Janssen, C. & Dresen, G., 2000. Fracture process zone in granite, *J. geophys. Res.,* **105**(B10), 23 651–23 661.

Zhang, J.Z., Zhou, X.P., Zhou, L.S. & Berto, F., 2019. Progressive failure of brittle rocks with non-isometric flaws: insights from acousto-optic-mechanical (AOM) data, *Fatigue Fract Eng. Mater. Struct.,* **42**(8), 1787–1802.

Zhang, Z.H., Deng, J.H., Zhu, J.B. & Li, L.R., 2018. An experimental investigation of the failure mechanisms of jointed and intact marble under compression based on quantitative analysis of acoustic emission waveforms, *Rock Mech, Rock Eng.,* **51**(7), 2299–2307.

Zhou, T., Zhu, J. & Xie, H., 2020a. Mechanical and volumetric fracturing behavior of three-dimensional printing rock-like samples under dynamic loading, *Rock Mech. Rock Eng.,* doi:10.1007/s00603-020-02084-5.

Zhou, X.P., Zhang, J.Z. & Wong, L.N.Y., 2018a. Experimental study on the growth, coalescence and wrapping behaviors of 3D cross-embedded flaws under uniaxial compression, *Rock Mech. Rock Eng.,* **51**(5), 1379–1400.

Zhou, X.P., Zhang, J.Z., Yang, L.H. & Cui, Y.L., 2018b. Internal morphology of cracking of two 3D pre-existing cross-embedded flaws under uniaxial compression, *Geotech. Test. J.,* **41**(2), 329–339.

Zhou, X.P., Zhang, J.Z. & Berto, F., 2020b. Fracture analysis in brittle sandstone by digital imaging and AE techniques: role of flaw length ratio, *J. Mater. Civ. Eng.,* **32**(5), 04020085.

Zhou, X.P., Zhang, J.Z. & He, Y., 2020c. Stick-slip failure in sheared fault with a variety of end constraint degrees: an experimental study, *Phys. Earth Planet Inter.,* **301,** doi:10.1016/j.pepi.2020.106454.

APPENDIX A: RESULTS OF THE REPEATED EXPERIMENTS

APPENDIX B: MECHANISMS FOR DAMAGE PROGRESSIONS IN FLAWED GRANITE

For flawed granite, the microtensile failure outperforms the microshear failure prior to the acoustic quiescence period due to the strong mineral grain shear strength and the large grain size (Morgan *et al.* 2013). However, during the relative acoustic quiescence period, the microshear failure mechanism is strengthened in the deforming specimen due to the propagation of macrocracks, and thus the microshear failure mechanism and the microtensile failure mechanism coexist and dictate the damage progressions in flawed granite (Yin *et al.* 2014; Zhang *et al.* 2019a). After the acoustic quiescence period, the macrocracks cease to grow, and the FPZs surrounding the tips of formed macrocracks continue to develop at the new stress buildup phase. In this state, microtensile failure prevails again in the deforming specimen. These interpretations can be demonstrated by the waveform-based analysis. Four exemplificative waveforms, together with their corresponding amplitude spectra, are presented in Fig. B1 to illustrate the potential driving mechanisms in damage progressions in flawed granite before, during and after the acoustic quiescence. The first waveform (Fig. B1a1) is typical of the waveforms recorded before the acoustic quiescence, and the second and the third waveforms (Figs B1b1 and c1) are typical of the waveforms recorded during the acoustic quiescence. Then, the fourth waveform (Fig. B1d1) is typical of the waveforms recorded after the acoustic quiescence.

Fig. B1 implies that the dominant frequency (i.e. the point where the power spectrum is greatest) of the first, second and fourth amplitude spectra reaches 90.13, 75 and 43.13 kHz, respectively, while the dominant frequency of the third amplitude spectrum attains 327.38 kHz. The first, the second and fourth amplitude spectra have a remarkably lower dominant frequency than the third amplitude spectrum. Waveforms of low dominant frequency (L-type AE signals) are produced by microtension failure, and waveforms of high dominant frequency (H-type AE signals) are caused by microshear failure (Li *et al.* 2017; Zhang *et al.* 2018). It is therefore indicated that the cracking behaviour in flawed granite before and after acoustic quiescence is dominated by microtensile failure, while due to the propagation of macrocracks, the microshear failure mechanism is remarkably strengthened in the deforming specimen during the relative acoustic quiescence period. Note that the amplitude of the L-type AE signal in Fig. B1(b1) is much higher than that in Figs B1(a1) and (d1), indicating that the microtensile failure mechanism is also strengthened during the relative acoustic quiescence period. This result suggests that microtensile failure mechanism and microshear failure mechanism co-exist at the moment of macrofracturing. The tensile-shear coexistence mechanism during the relative acoustic quiescence period is consistent with the optical observations in Table 4(b), and is also in good agreement with the experimental observations by Brooks *et al.* (2013), Yin *et al.* (2014) and Zhang *et al.* (2019a). Additionally, the L-type AE signal has an amplitude considerably higher than the H-type AE signal, while it is also characterized by a shorter duration (also rise time) (Figs B1a1, b1, d1 compared to Fig. B1c1). These waveform features are in good agreement with the findings of Aggelis *et al.* (2013a) and faithfully confirm the characteristics of typical AE parameters presented in Fig. 9.

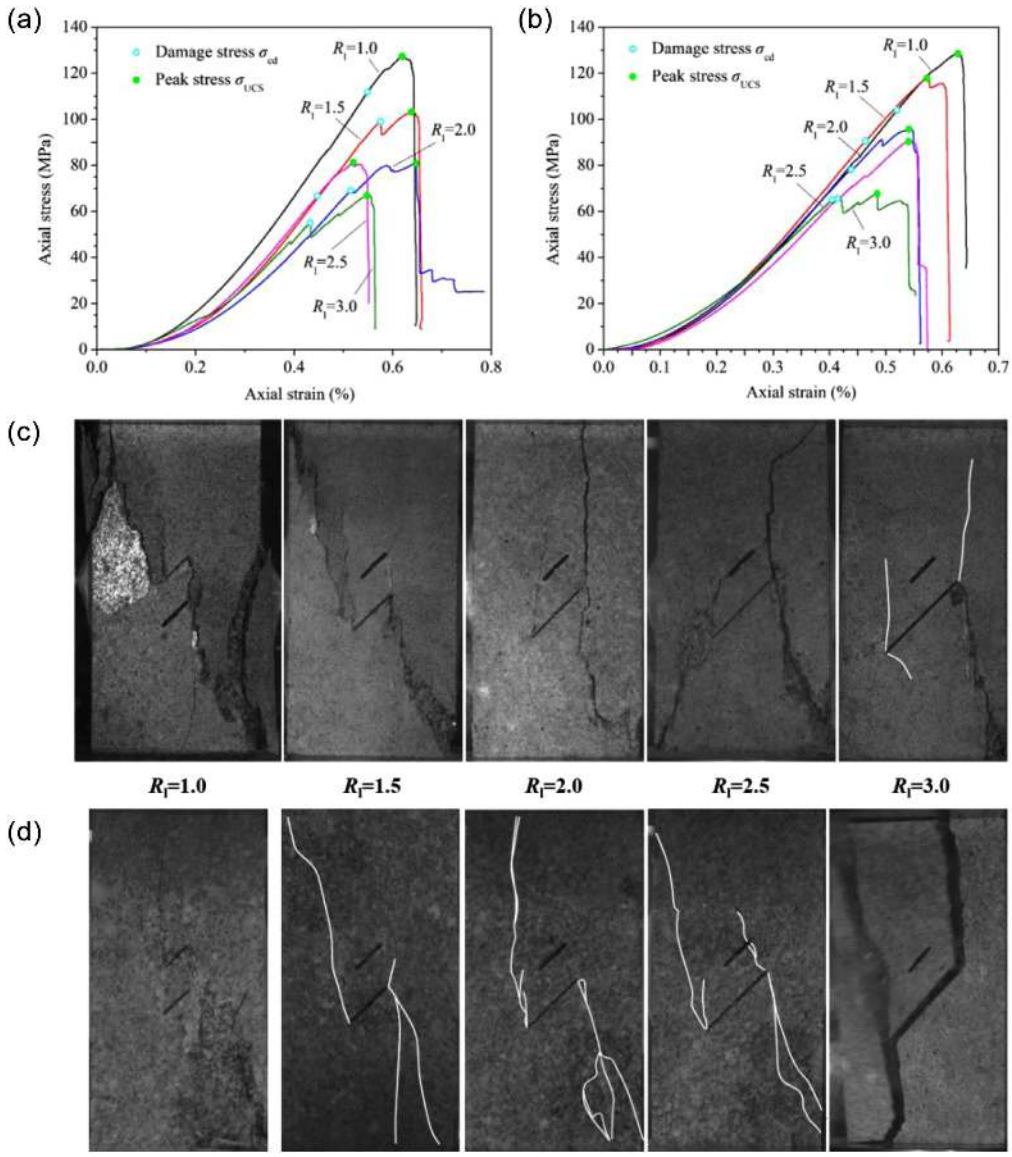

Figure A1. Axial stress–strain curves in (a) the second and (b) the third experiments, and ultimate failure modes in (c) the second and (d) the third experiments of each flaw length ratio. The hollow dot in Figs A1(a)–(b) denotes damage stress, and the solid dot denotes peak stress. White lines in Figs A1(c)–(d) are delineated to clearly define the growth paths of narrower macrocracks at failure.

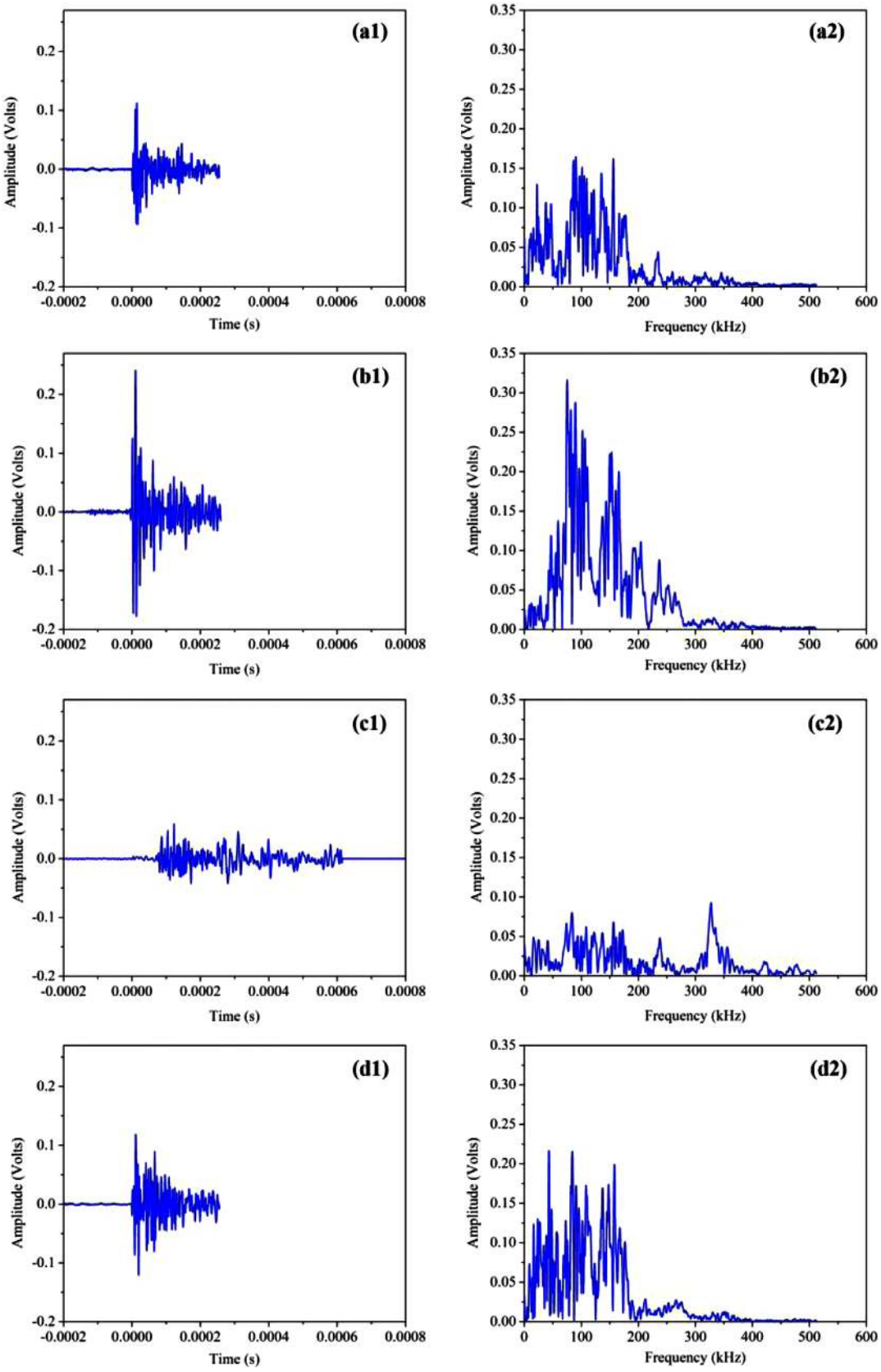

Figure B1. (a1, b1, d1) L-type AE signals and (c1) H-type AE signal recorded (a1) before, (b1, c1) during and (d1) after the second acoustic quiescence period, along with their corresponding amplitude spectra (a2–d2), in the flawed granite specimen with $R_1 = 1.5$.